

Effect of electron-phonon interaction on spectroscopies in graphene

J. P. Carbotte

*Department of Physics and Astronomy, McMaster University, Hamilton, Ontario, Canada L8S 4M1
and The Canadian Institute for Advanced Research, Toronto, Ontario, Canada M5G 1Z8*

E. J. Nicol*

Department of Physics, University of Guelph, Guelph, Ontario, Canada N1G 2W1

S. G. Sharapov

*Bogolyubov Institute for Theoretical Physics, 14-b Metrologicheskaya Street, Kiev 03680, Ukraine
(Received 17 August 2009; revised manuscript received 28 October 2009; published 19 January 2010)*

We calculate the effect of the electron-phonon interaction on the electronic density of states (DOS), the quasiparticle properties, and on the optical conductivity of graphene. In metals with DOS constant on the scale of phonon energies, the electron-phonon renormalizations drop out of the dressed DOS, however, due to the Dirac nature of the electron dynamics in graphene, the band DOS is linear in energy and phonon structures remain, which can be emphasized by taking an energy derivative. There is a shift in the chemical potential and in the position in energy of the Dirac point. Also, the DOS can be changed from a linear dependence out of value zero at the Dirac point to quadratic out of a finite value. The optical scattering rate $1/\tau$ sets the energy scale for the rise of the optical conductivity from its universal dc value $4e^2/\pi h$ (expected in the simplest theory when chemical potential and temperature are both $\ll 1/2\tau$) to its universal ac background value ($\sigma_0 = \pi e^2/2h$). As in ordinary metals the dc conductivity remains unrenormalized while its ac value is changed. The optical spectral weight under the intraband Drude is reduced by a mass-renormalization factor as is the effective scattering rate. Optical weight is transferred to an Holstein phonon-assisted side band. Due to Pauli blocking the interband transitions are sharply suppressed, but also nearly constant, below twice the value of renormalized chemical potential and also exhibit a phonon-assisted contribution. The universal background conductivity is reduced below σ_0 at large energies.

DOI: [10.1103/PhysRevB.81.045419](https://doi.org/10.1103/PhysRevB.81.045419)

PACS number(s): 78.67.-n, 71.38.Cn, 73.40.Gk, 81.05.U-

I. INTRODUCTION

Graphene consists of a monolayer of a honeycomb lattice of carbon atoms. It has been studied theoretically since the early work of Wallace.¹ An important aspect of the charge dynamics in graphene is that it is governed by a Dirac rather than a Schrödinger equation. Fermionic energies are proportional to momentum with the effective speed of light $v_0 \approx 10^6$ m/s. While the material was isolated experimentally only in 2004,^{2,3} many fascinating discoveries have already appeared⁴⁻⁶ including an integer quantum-Hall effect with half-integer filling factors, a minimum conductivity and a Berry phase shift of π .⁶⁻⁹

An important dimension in the study of graphene is that it can be incorporated into a field-effect device⁶ and doped away from half filling by changing the gate voltage. This means that the position of the chemical potential can be varied with respect to the Dirac point where conical valence and conduction band meet at two specific K points in the Brillouin zone. As is the case in ordinary metals the electron-phonon interaction (EPI) (Refs. 10 and 11) renormalizes the bare bands and changes the properties of graphene. Here we consider specifically the electronic density of states (DOS). In metals, where the DOS is essentially energy independent on the scale of phonon energies, a well-known result is that the electron-phonon self-energy entirely drops out of the problem and the DOS retains its bare value. In graphene, as we will show in this paper, this is no longer the case and there is an imprint of the EPI in the renormalized DOS. This is expected in systems where the DOS varies on an energy

scale comparable to phonon energies.¹² It also arises in finite band systems with the top and the bottom of the band are modified in a particularly important way by interactions with the phonons.¹³⁻¹⁶

Another known result in simple metals is that the EPI renormalizations^{10,11,17} drop out of the dc value of the conductivity but significantly renormalize its ac value and phonon-assisted Holstein processes become possible. For graphene the dc conductivity which is due to both intraband and interband transitions is also unaffected by the EPI. However, the intraband ac Drude contribution has its optical spectral weight reduced by a factor of $(1 + \lambda^{\text{eff}})$, where λ^{eff} is the effective-mass-renormalization parameter (dependent on the value of the chemical potential) and its scattering rate is also reduced by the same factor. Optical spectral weight is shifted to phonon-assisted Holstein side bands originating from the incoherent part of the electron spectral density. The interband transitions, which are strongly suppressed by Pauli blocking below twice the renormalized chemical potential, also exhibit phonon-assisted side bands which add on to the intraband Holstein processes at photon energies above the phonon energy. The universal value of the background conductivity at higher energies is suppressed below its bare-band value $\sigma_0 = \pi e^2/2h$.

In Sec. II, we introduce the model of Park *et al.*¹⁸⁻²⁰ for the electron-phonon interaction in graphene which we write in a more general form so as to include the self-consistent electronic DOS in the self-energy itself. Iterations of the self-energy to obtain a self-consistent value of the DOS is known to be important in finite bands particularly in the region of

the band edge. The electron-phonon interaction renormalizes the electronic motion at the Fermi surface through a renormalization factor $(1+\lambda^{\text{eff}})$.²¹ In addition, the chemical potential is changed from its bare-band value as is the relative position of the Dirac point. In the limit of small chemical potential, analytic formulas are obtained for these renormalizations and are compared with more general numerical results. Our results for the renormalized DOS show phonon signatures at small energies and a renormalization of the band edge with renormalized bands no longer ending abruptly as in the bare band. An analytic formula is derived for the modification in the Dirac point due to interactions.

In Sec. III, we consider more specifically phonon structure in the renormalized DOS, a topic on which we have some preliminary and complementary work.²² To this end, we introduce a Lorentzian model for the phonon distribution instead of the simple Einstein model of Park *et al.*¹⁸ This provides a more realistic description of the structure that is expected to be seen in experiment.²³ To see this structure more clearly, we take a first derivative and find that the Lorentzian line shape of our assumed boson spectrum is faithfully reproduced in these plots except for a small shift in energy. Section IV deals with aspects of quasiparticle renormalization as they show up in angle-resolved photoemission spectra (ARPES).^{24–27} We particularly emphasize the shift in chemical potential²⁸ revealed in such curves and note that electron-phonon renormalizations remain to high energies. Section V deals with optical conductivity^{29–39} starting with the effect of the electron-phonon renormalization on the low-frequency conductivity. We begin with the dc conductivity which is found to be unrenormalized. Conditions for the observation of the universal limit are discussed and the contribution to this value of intraband and interband transitions are separately determined. The rise of the conductivity $\sigma(\Omega)$ from its universal dc to its universal ac background value³⁵ with increasing frequency Ω is described. Analytic formulas are provided for the electron-phonon renormalization that arises for finite doping when μ is much larger than the impurity scattering rate $1/\tau$. We find that in this case, the intraband transitions provide a Drude-type contribution to the conductivity which, just as is known to be the case in ordinary metals,¹⁷ is renormalized by the mass-enhancement factor $(1+\lambda^{\text{eff}})$ in two ways. The effective plasma frequency of the Drude as compared to its free band case is reduced by $1/(1+\lambda^{\text{eff}})$ and the scattering rate $1/\tau$ also goes into $(1/\tau)/(1+\lambda^{\text{eff}})$. In addition, optical spectral weight is transferred into Holstein phonon-assisted absorption sidebands. On the other hand and in sharp contrast, the interband transitions at small Ω remain unrenormalized but beyond the phonon energy also exhibit Holstein sidebands. In Sec. VII, the infrared region of the conductivity^{40–43} is considered more explicitly with the specific aim of understanding separately the role played by intraband and interband transitions. It is explained how interband transitions which would be Pauli blocked in the pure bare band case can nevertheless take place in the interacting system although with reduced spectral weight. This arises because in the interacting system Bloch states are never occupied with probability one and so Pauli blocking is not complete. The partial sum rule on the optical conductivity is discussed. Section VIII contains a

summary and conclusions. Finally, an Appendix is provided where a list is made of our main results for graphene in comparison with conventional metals.

II. THEORETICAL BACKGROUND

In graphene, the massless Dirac nature of the electrons means that their energy ($\epsilon_{\mathbf{k}}$) is linear in momentum ($\hbar\mathbf{k}$) and consists of two branches, i.e., $\epsilon_{\mathbf{k}} = \pm \hbar v_0 |\mathbf{k}|$ with the velocity v_0 equal to about 10^6 m/sec and \mathbf{k} as the wave vector measured from one of the two K points in the Brillouin zone where valence and conduction bands meet. The \pm corresponds to the upper and lower Dirac cones or particles and holes, respectively. Here, ϵ can serve as the label for the absolute value of momentum. The carrier spectral density $A(\epsilon, \omega)$ can be written in terms of the self-energy $\Sigma(\omega)$ as

$$A(\epsilon, \omega) = \frac{1}{\pi} \frac{-\text{Im} \Sigma(\omega)}{[\omega - \text{Re} \Sigma(\omega) + \mu - \epsilon]^2 + [\text{Im} \Sigma(\omega)]^2}. \quad (1)$$

Valence and conduction cones are both part of Eq. (1) and correspond, respectively, to negative and positive ϵ label. As defined, $\Sigma(\omega)$ is the self-energy such that $\omega=0$ corresponds to the Fermi level and μ is the chemical potential of the interacting system. The electron-phonon interaction in graphene has been discussed by many authors^{18,24,26} including recent work^{32–34} directed toward understanding its effect on the optical conductivity. Here we find it convenient to follow the formulation of Park *et al.*¹⁸ later also generalized to bilayers and graphite.¹⁹ These authors proceed within an *ab initio* pseudopotential density-functional calculation of the electronic bands in the local-density approximation (LDA). They further calculate the phonon frequencies and polarization as well as the electron-phonon matrix elements from which they construct the electron self-energy. The importance of this work to the present discussion is that in the end they provide a simplified model for the self-energy which they find captures all essential elements of their sophisticated numerical calculations. They show that to a good approximation, one can think of the electrons as coupled to a single phonon of frequency $\omega_E=200$ meV and provide a value for the relevant coupling. The self-energy is independent of electron momentum label as well as band index, electrons or holes, a simplification they trace¹⁹ to the Dirac nature of the electronic states in graphene. Based on these simplifying ideas, we begin with a self-energy for temperature $T=0$ of the form^{13,14}

$$\Sigma(\omega) = \int_{-\infty}^{+\infty} d\omega' \frac{N(\omega')}{N_0} \frac{A}{W_C} \left[\frac{\theta(\omega')}{\omega - \omega' - \omega_E + i0^+} + \frac{\theta(-\omega')}{\omega - \omega' + \omega_E + i0^+} \right]. \quad (2)$$

In Eq. (2), ω_E is the Einstein oscillator energy, ω is in units of energy, A is the coupling, $\theta(\omega)$ is the Heaviside function, and $N_0=2/\pi\hbar^2v_0^2$. W_C is the cutoff on the Dirac cone given by $\sqrt{\pi}\sqrt{3}t$, with t as the nearest-neighbor hopping parameter taken to be 3 eV which corresponds to $W_C \approx 7000$ meV. In Eq. (2), we have added an additional element not included in

the previous work of Park *et al.*¹⁸ but which can be important in the case of graphene: $N(\omega)$ is the *self-consistent* electronic density of states given by

$$\frac{N(\omega)}{N_0} = \int_{-W_C}^{W_C} d\epsilon \frac{|\epsilon|}{\pi} \frac{-\text{Im} \Sigma(\omega)}{[\omega - \text{Re} \Sigma(\omega) + \mu - \epsilon]^2 + [\text{Im} \Sigma(\omega)]^2}. \quad (3)$$

This can be evaluated analytically to give a useful formula shown in Ref. 22. In good metals, the electronic DOS in the energy range important for the electron-phonon interaction around the Fermi energy, does not vary significantly. Only its value at the chemical potential is relevant. In such systems, the linear in ϵ factor $|\epsilon|$ is not present in Eq. (3) and extending the integration limits to infinity gives a constant independent of $\text{Im} \Sigma(\omega)$ and $\text{Re} \Sigma(\omega)$. In more complicated metals such as the A15 compounds, as an example, it was recognized early on that such an approximation is no longer valid¹² and in this instance it is the self-consistent DOS (Refs. 13–15) that enters Eq. (2), as in the work of Engelsberg and Schrieffer.¹⁶ This is also relevant for finite bands. In particular, a sharp band edge in the electronic density of states $N(\omega)$ becomes broadened by interactions and consequently tails arise at energies beyond the bare-band cutoff. But conservation of states on $N(\omega)$ imply that compensating decreases must occur at other energies. For the electron-phonon interaction, these changes extend to the phonon energy region.^{14,15} For graphene, the bare-band-structure density of states is linear in energy rather than constant and hence we expect significant changes could be introduced into $\Sigma(\omega)$ when Eqs. (2) and (3) are iterated to convergence. We will test this in what follows.

As a first approximation, we can replace $N(\omega)$ in Eq. (2) by its bare noninteracting value given by

$$\frac{N(\omega)}{N_0} = \begin{cases} |\omega + \mu_0| & \text{for } -W_C - \mu_0 < \omega < W_C - \mu_0 \\ 0 & \text{otherwise,} \end{cases} \quad (4)$$

where μ_0 is the chemical potential for the bare bands, i.e., without electron-phonon renormalization. All states with $\omega < 0$ are occupied and with $\omega > 0$ unoccupied so that $\omega=0$ sets the boundary between occupied and unoccupied energies, and by choice this remains the case even when interactions are included. Note that the value of μ_0 sets the doping ρ (per unit area) with $\rho = \text{sgn}(\mu_0) \mu_0^2 / (\pi \hbar^2 v_0^2)$ with μ_0 nega-

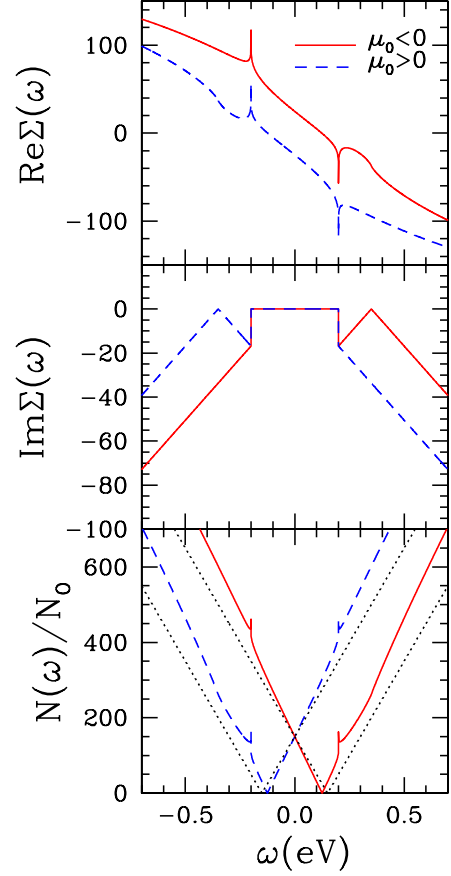


FIG. 1. (Color online) Real (top) and imaginary (middle) part of the self-energy $\Sigma(\omega)$ and the density of states $N(\omega)/N_0$ (bottom) (all in units of meV) as a function of ω in eV for $|\mu_0|=150$ meV. Dashed is for $\mu_0 > 0$ and solid is for $\mu_0 < 0$. The bare-band DOS is indicated by the dotted curve.

tive for holes and positive for electrons. This is illustrated in the bottom frame of Fig. 1 by the black dotted lines for the case of $|\mu_0|=150$ meV. The Dirac point is at -150 meV ($+150$ meV) for electron (hole) doping and corresponds to zero DOS or $\omega = -\mu_0$ from Eq. (4). For this bare $N(\omega)$ the self-energy of Eq. (2) can be evaluated analytically but is different for $\mu_0 > 0$ and $\mu_0 < 0$. For $\mu_0 > 0$ [writing $\Sigma_{\mu_0 > 0}(\omega)$

$$\text{Re} \Sigma_{\mu_0 > 0}(\omega) = \frac{A}{W_C} \left\{ \omega_E \ln \left| \frac{(W_C + \omega_E - \omega - \mu_0)(\mu_0 + \omega + \omega_E)^2}{(\omega^2 - \omega_E^2)(W_C + \omega + \omega_E + \mu_0)} \right| - (\mu_0 + \omega) \ln \left| \frac{(W_C + \omega_E - \omega - \mu_0)(W_C + \omega + \omega_E + \mu_0)(\omega + \omega_E)}{(\omega - \omega_E)(\omega + \mu_0 + \omega_E)^2} \right| \right\} \quad (5)$$

and for negative μ_0 , $\text{Re} \Sigma_{\mu_0 < 0}(\omega) = -\text{Re} \Sigma_{|\mu_0|}(-\omega)$. This symmetry between positive and negative values of chemical po-

tential also holds in the case when the full self-consistent DOS $N(\omega')$ is used in Eq. (2). The imaginary part is

$$-\text{Im } \Sigma(\omega) = \begin{cases} \frac{\pi A}{W_C} |\omega - \omega_E + \mu_0| & \text{for } \omega_E < \omega < W_C - \mu_0 + \omega_E \\ \frac{\pi A}{W_C} |\omega + \omega_E + \mu_0| & \text{for } -\omega_E > \omega > -W_C - \mu_0 - \omega_E \end{cases} \quad (6)$$

and zero outside these intervals. For negative values of μ_0 , $\text{Im } \Sigma_{\mu_0 < 0}(\omega) = \text{Im } \Sigma_{|\mu_0|}(-\omega)$. And for the self-consistent DOS, we see that $N_{\mu_0 < 0}(\omega) = N_{|\mu_0|}(-\omega)$ and this relationship implies that the symmetries of Eqs. (5) and (6) apply even when the full self-consistent DOS is used in Eq. (2) for the self-energy.

In Fig. 1, we show results for $\text{Re } \Sigma(\omega)$ (top frame), $\text{Im } \Sigma(\omega)$ (middle frame), and $N(\omega)/N_0$ (bottom frame), where $N(\omega)$ is a first iteration of Eq. (2) which should be sufficient for small enough electron-phonon interaction. The dashed (blue) lines are for $\mu_0 > 0$ (electron doping) and the solid (red) for $\mu_0 < 0$ (hole doping). The dotted (black) line in the bottom frame is the bare-band density of states shown for comparison. Here the chemical potential μ_0 was taken to be $|\mu_0| = 150$ meV, $W_C = 7000$ meV, and ω_E was taken to be 200 meV as in Ref. 18. The value of the electron-phonon A parameter was set at 250 meV. The corresponding spectral mass enhancement $\lambda \equiv 2A/\omega_E = 2.5$. As we will show, this parameter is very different from the true mass enhancement which we will call λ^{eff} and which describes for graphene the renormalization of the velocity because the carriers are massless.

Note that the symmetry incorporated into Eq. (5) is satisfied in the top frame for $\text{Re } \Sigma(\omega)$. We see logarithmic-type singularities¹³ at $\omega = \pm \omega_E$ but these would be smeared if one had used a distributed phonon spectra rather than an Einstein model. The logarithmic singularity can be traced to a factor $(\omega \pm \omega_E)$ in the argument of the logarithm in Eq. (5) and these will lead to sharp structure in the electronic density of states. For later reference, we note an important exception. For zero chemical potential $\mu_0 = 0$, cancellations occur in Eq. (5) and the singularities are removed.

$\text{Re } \Sigma(\omega=0)$ is not zero but -24.7 ($+24.7$) meV for $\mu_0 > 0$ ($\mu_0 < 0$). This quantity relates interacting (μ) and non-interacting (μ_0) chemical potential^{12,16,28} with

$$\mu = \mu_0 + \text{Re } \Sigma(\omega=0). \quad (7)$$

If for simplicity we assume all three energy scales ω , μ , and ω_E to be small as compared with the large band cutoff W_C , and for $\mu_0 \ll \omega_E$, we can show⁴⁴ the renormalized energy (E_k) as measured, for example, in ARPES is related to the bare energy near the Fermi energy by

$$E_k = \frac{\epsilon_k - \epsilon_{k_F}}{1 + \lambda^{\text{eff}}} = \frac{\pm \hbar v_0(k - k_F)}{1 + \lambda^{\text{eff}}} \quad (8)$$

with $\hbar k_F$ as the Fermi momentum of the bare band, so $\mu_0 = \pm \hbar v_0 k_F$, with the $+$ sign for electron doping and $-$ for holes. We see that interactions renormalize the bare effective speed of light v_0 to $v_0^* = v_0/(1 + \lambda^{\text{eff}})$. Here

$$\lambda^{\text{eff}} = \frac{2A}{W_C} \left[\ln \left| \frac{W_C}{\omega_E} \right| - 1 \right], \quad (9)$$

which is ~ 0.19 for the parameters of Fig. 1. This value is larger than calculated in density-functional theory¹⁸ but smaller than measured experimentally.²⁵ Also

$$\mu = \mu_0(1 - \lambda^{\text{eff}}) \simeq \frac{\mu_0}{1 + \lambda^{\text{eff}}}. \quad (10)$$

The middle frame of Fig. 1 gives first iteration results for the imaginary part [$\text{Im } \Sigma(\omega)$] of the self-energy which clearly satisfy the symmetry of Eq. (6). $\text{Im } \Sigma(\omega)$ is zero between $-\omega_E < \omega < \omega_E$ at which point it jumps up to a finite value because only then can a quasiparticle decay by boson emission. In an ordinary metal the scattering would remain constant above ω_E because the final density of electronic states at $\omega - \omega_E$ is constant. This is not true for graphene where $N(\omega - \omega_E)$ varies and the scattering rate reflects the energy dependence of the underlying bare band structure seen in the lower frame of Fig. 1 as the black dotted curve. Looking at the red solid curve for energy less than ω_E , the $|\text{Im } \Sigma(\omega)|$ increases linearly with ω as does $N_0(\omega)$ and for $\omega > \omega_E$ we see first a drop toward the zero in $|\text{Im } \Sigma(\omega)|$ after which it too increases linearly, imaging the bare density of states as captured in Eq. (6). In more realistic calculations there would be a nonzero contribution to the self-energy from acoustic phonons and $\text{Im } \Sigma(\omega)$ would never be exactly zero as we have it here. But from the work of Ref. 18, this is small in graphene. Finally, we note that for a fixed value of $\pm \mu_0$, $\text{Im } \Sigma(\omega)$ is not symmetric with respect to $\omega \rightarrow -\omega$ as it would be in good metals. Here such a symmetry results only when $\mu_0 = 0$, i.e., the case of no doping.

In the lower frame of Fig. 1, we show our one iteration results for the DOS $N(\omega)$ (solid red curve for $\mu_0 < 0$ and dashed blue for $\mu_0 > 0$) and compare with the bare case (dotted black curves). $N(\omega)$ is not symmetric about $\omega = 0$ and the renormalizations are not the same for electron and hole branches. Also, the Dirac point is shifted to higher energy as compared to its bare-band position for $\mu_0 > 0$ and to lower energy for $\mu_0 < 0$. The shift becomes greater with increased doping. Another feature to notice is that bare and renormalized DOS have exactly the same value at $\omega = 0$, which is where by choice we have taken the Fermi level to be in both cases. This makes sense because the imaginary part of $\Sigma(\omega)$ at $\omega = 0$ is always zero and so the Lorentzian forms in Eq. (3) reduce to delta functions and for $\mu_0 > 0$, as an example

$$\frac{N(\omega=0)}{N_0} = \mu - \text{Re } \Sigma(\omega=0) = \mu_0, \quad (11)$$

which is the value of the bare density of states at the bare chemical potential. The value of the DOS at the Fermi surface remains pinned to its noninteracting value. Another important feature of our DOS results is that phonon structures are clearly seen as small kinks in the curve. This will be smeared somewhat when a distributed spectrum is used in computing the self-energy rather than the Einstein mode of Eq. (2). We will return to this issue in a later section where we focus more specifically on phonon structures. For the

moment, we note that our results for $N(\omega)$ versus ω are in striking contrast to what is found to apply in conventional metals. In that case, the density of electronics states around the Fermi surface is constant on the scale of a few times the phonon energy and no renormalization of the DOS due to the electron-phonon interaction is expected or observed. Further in conventional metals, the energy bands are rigidly filled as the chemical potential is varied. For graphene, when coupling to a boson spectrum is included, the bands become renormalized differently for *each value* of the chemical potential μ_0 . These are not *rigid* bands.

Next we look at how the position of the Dirac point shifts from its bare value at $\omega = -\mu_0$ when interactions are included. In the interacting system, the Dirac point can still be identified with zero momentum $k=0$ (momentum label) which corresponds to $\epsilon=0$ (energy label) as $\epsilon = \pm \hbar v_0 |\mathbf{k}|$. If there was no broadening (but of course there is), the spectral function would become infinite (peaks) at $\omega - \text{Re } \Sigma(\omega) + \mu = 0$. If we write

$$\text{Re } \Sigma(\omega) = \text{Re } \Sigma(\omega=0) + \text{Re } \delta\Sigma(\omega), \quad (12)$$

where $\text{Re } \delta\Sigma(\omega)=0$ at $\omega=0$ by arrangement, we get

$$\omega - \text{Re } \Sigma(\omega=0) + \mu - \text{Re } \delta\Sigma(\omega) = 0 \quad (13)$$

as the transcendental equation which needs to be solved to obtain the energy of the Dirac point in the interacting band. For one iteration, $\text{Re } \Sigma(\omega)$ is given by Eq. (5) from which $\text{Re } \delta\Sigma(\omega)$ can easily be extracted. Noting Eq. (7), Eq. (13) simplifies to

$$\omega_d = -\mu_0 + \text{Re } \delta\Sigma(\omega_d), \quad (14)$$

where ω_d is the energy of the Dirac point in the interacting system. For the bare band case $\text{Re } \delta\Sigma(\omega_d)$ in Eq. (14) is zero and we recover the known result that the Dirac point is at $-\mu_0$. $\text{Re } \delta\Sigma(\omega_d)$ which we plot as a function of μ_0 in the middle frame of Fig. 2 gives the shift in ω_d away from $-\mu_0$ resulting from the electron-phonon interaction. It has the same sign as μ_0 and hence displaces the Dirac point to the right of its bare value for $\mu_0 > 0$ and to the left for $\mu_0 < 0$ as we noted before. In the upper frame of Fig. 2 we show a related quantity, namely, $\text{Re } \Sigma(\omega=0)$ which is the shift in chemical potential (μ) from its bare-band value (μ_0). It carries the opposite sign to μ_0 and so shifts μ to the left of μ_0 for positive μ_0 and vice versa for negative μ_0 . This shift in chemical potential is expected because the interactions modify the density of states and hence to keep the carrier imbalance fixed, the position of the Fermi level needs to be modified. The question of how this shift might manifest itself will be addressed in a later section. Shifts in the Dirac point position can be seen in ARPES (Ref. 25) and in scanning-tunneling microscopy (STM).⁴⁵ Noting that the electron-phonon interaction makes only a small contribution to the measured total quasiparticle scattering rates²⁰ seen in graphene and that the electron-electron interactions are needed to understand these, i.e., particle hole and plasmons,²⁰ any conclusive comparison with experiment would need to include these additional interactions and so we do not attempt here a comparison with data. Before leaving this section, we note that for $\mu_0 \ll \omega_E$ we can show that

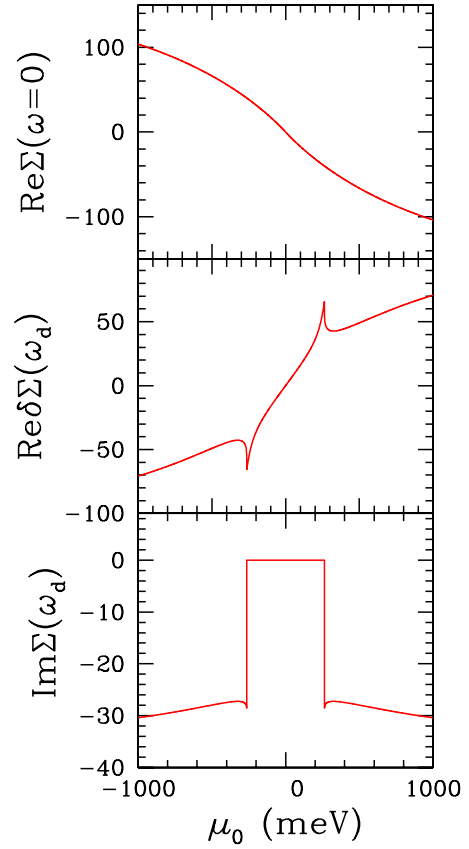


FIG. 2. (Color online) Results of a first iteration for the shift in chemical potential $\text{Re } \Sigma(\omega=0)$ (top frame), the shift in position of the Dirac point $\text{Re } \delta\Sigma(\omega_d)$ (middle frame), and the imaginary part of the self-energy $\text{Im } \Sigma(\omega_d)$ at the Dirac point (lower frame). All of these quantities are shown in units of meV.

$$\omega_d \simeq -\frac{\mu_0}{1 + \lambda^{\text{eff}}} \quad (15)$$

from Eq. (14) with $\text{Re } \delta\Sigma(\omega_d)$ replaced by $\text{Re } \delta\Sigma(-\mu_0)$. Again, to a first approximation, the $(1 + \lambda^{\text{eff}})$ factor renormalizes the position in energy of the Dirac point. In this approximation, the magnitude of ω_d , i.e., $|\omega_d|$, is equal to the magnitude of the renormalized chemical potential $|\mu|$. Except for prominent phonon structures seen in the middle of Fig. 2, not present in the top frame, $|\text{Re } \delta\Sigma(\omega_d)|$ and $|\text{Re } \Sigma(\omega=0)|$ are not very different in magnitude as compared with the magnitude of μ itself and so renormalized values of $|\omega_d|$ and $|\mu|$ are close to each other, even for a general value of chemical potential.

In Fig. 3, we consider the case of $\mu_0 = 500$ meV and compare our initial step uniterated results shown as the dashed lines with results obtained (solid curves) when DOS [Eq. (3)] and self-energy [Eq. (2)] are iterated to convergence. We see some changes in real and imaginary part of $\Sigma(\omega)$ top and middle frames, respectively. We note however that the change in slope of the $\text{Re } \Sigma(\omega)$ out of zero is not changed much in the solid curve which means that the one iteration estimate of the effective-mass renormalization λ^{eff} is quite good. Results for λ^{eff} are shown in Fig. 4 as a function of μ_0 .

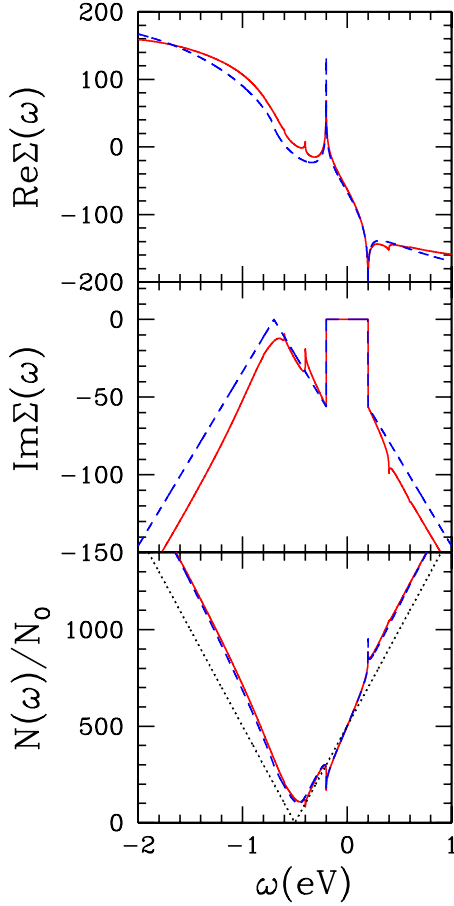


FIG. 3. (Color online) Same quantities as for Fig. 1 but now the self-energy and density of states have been self-consistently iterated and $\mu_0=500$ meV which is greater than ω_E . The solid curves are for the iterated case and the dashed curves are for the initial uniterated results. The dotted curve is the bare density of states. All quantities on the y axis are in meV.

Its value increases by a factor of 2 over the range shown.

The differences between iterated and noniterated results for the $-\text{Im} \Sigma(\omega)$ shown in the middle frame of Fig. 3 are larger and can become significant. It is clear that self-consistency could be important in some quantitative estimation of electron-phonon effects on the quasiparticle scattering rate and that LDA can underestimate these in some cases. There are also changes in the resulting DOS shown in the bottom frame but these are small in the case shown. Effects of self-consistency become essential, however, when the band edge is considered. Figure 5 is the same as Fig. 3 but now the entire band width is shown within the linearized Dirac cone approximation with cutoff W_C . On this scale the phonon structures visible as sharp peaks in Fig. 3 are hardly seen. Note that in the one iteration case the imaginary part of $\Sigma(\omega)$ (middle frame) dashed curve becomes zero at the bare-band edge because the DOS runs out at this point but the solid curve which results when we iterate remains finite outside this range before eventually going to zero. These features of the renormalization get reflected in the density of state shown in the lower frame of Fig. 5 in which we have also added for reference the bare DOS $N_0(\omega)$ as the dotted

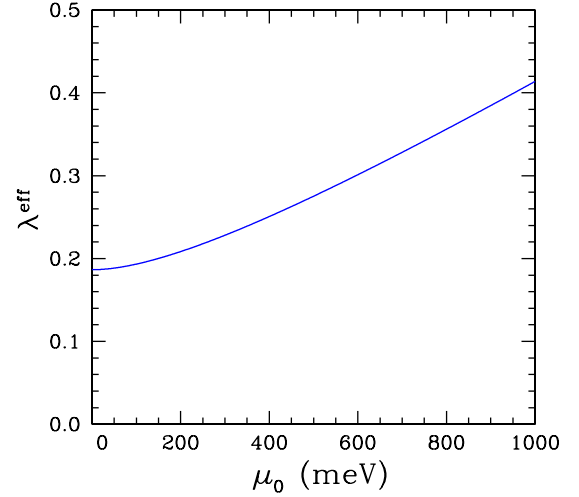


FIG. 4. (Color online) The mass-renormalization parameter λ^{eff} at the Fermi level as a function of bare chemical potential μ_0 .

(black) curve. It is clear that the electron-phonon interaction profoundly renormalizes the band edge. These effects have been studied before for other models of finite bands in, for example, Refs. 13–15. To obtain a good characterization of the renormalized band profile (red curve) around the bare-band edge W_C , it is essential to iterate.^{13,15} In a fully realistic model of graphene, one should, of course, use tight-binding

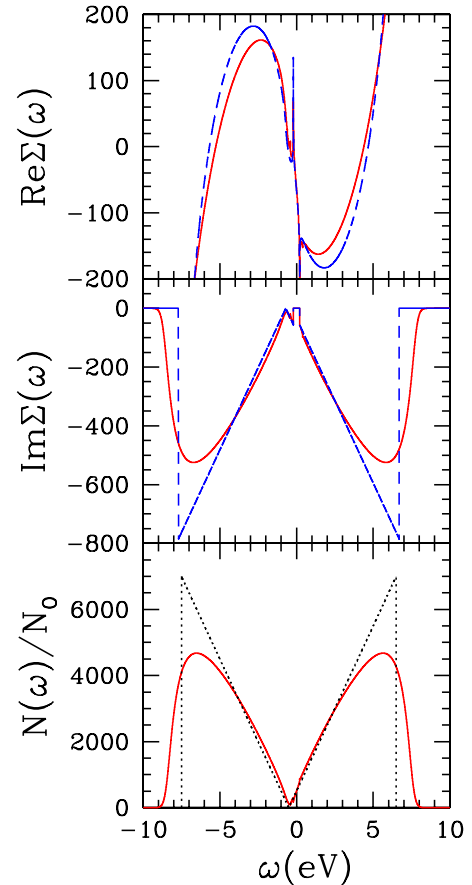


FIG. 5. (Color online) Same as for Fig. 3 but shown over a larger range of ω spanning the band edge.

bands as the Dirac cone approximation begins to fail at higher energies but band renormalization effects will occur in that case as well. We note that the top of the renormalized band extends to higher energies as compared with the bare band and the bottom extends to lower energies. It is the phonon energy which sets the scale for this smearing beyond the bare-band edge. Of course the total number of states must be preserved, i.e., the area under $N(\omega)/N_0$ is the same for bare (dotted black) and renormalized (solid red) curves. Due to interactions, i.e., damping, the states below W_C get depleted and so must reappear at higher energies leading to an increase in the effective band width. We have verified that to within our numerical accuracy the sum rule on $N(\omega)/N_0$ was indeed satisfied. As the bands distort, and these distortions are different for every choice of chemical potential μ_0 , it is clear that the Fermi level will also need to be shifted. Again, to within the accuracy of our numerical work, we have verified in a few instances that integration of the occupied part of the states up to μ given by Eq. (7) does give the right charge imbalance ρ .

Returning to ω of order, at most, a few times ω_E , a different point is illustrated in Fig. 6, where we compare results for the DOS for the case of Fig. 1 with $\mu_0 < \omega_E$ (top frame) with a case in which all parameters are kept the same but a value of $\mu_0 > \omega_E$, namely, $\mu_0 = 500$ meV is used. In the top frame the DOS at the Dirac point remains zero because for $\mu_0 = 150$ meV, the imaginary part of $\Sigma(\omega)$ is still zero at the energy of the Dirac point as is shown in the bottom frame of Fig. 2. But in the bottom frame for $\mu_0 = 500$ meV, this is no longer the case and the Dirac point becomes smeared and $N(\omega_d)$ is finite. Note that the shift between Dirac point position for bare and interacting bands has increased as compared to the case of the top frame (see middle frame of Fig.

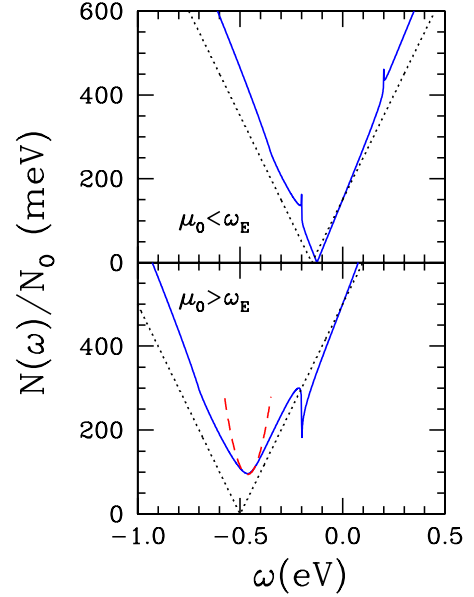


FIG. 6. (Color online) The density of states $N(\omega)$ (solid line) vs ω for $\omega_E = 200$ meV, $\lambda = 2.5$, and $W_C = 7000$ meV. The top frame is for $\mu_0 = 150$ meV $< \omega_E$ and the bottom for $\mu_0 = 500$ meV $> \omega_E$. The dotted curve is the bare-band case. For $\mu_0 > \omega_E$, $N(\omega)$ at the Dirac point is nonzero and becomes quadratic. A comparison of this approximate quadratic behavior given in Eq. (18) is shown as the dashed (red) curve.

2). It is useful to get a simple analytic expression for the DOS around the Dirac point.

For ω near ω_d and ϵ near $\epsilon = 0$, the spectral functions that determine the DOS are

$$A(\pm \epsilon, \omega) \approx \frac{1}{\pi} \frac{-\text{Im} \Sigma(\omega_d)}{[\omega - \text{Re} \Sigma(\omega_d) - \text{Re} \Sigma'(\omega_d)(\omega - \omega_d) + \mu \pm \epsilon]^2 + [\text{Im} \Sigma(\omega_d)]^2}. \quad (16)$$

Denoting $1 - \text{Re} \Sigma'(\omega_d)$ by Z , where $\Sigma'(\omega_d) \equiv d\Sigma(\omega)/d\omega|_{\omega=\omega_d}$, and $-\text{Im} \Sigma(\omega_d)$ by Γ , we obtain

$$A(\pm \epsilon, \omega) \approx \frac{1}{\pi} \frac{\Gamma}{[(\omega - \omega_d)Z \pm \epsilon]^2 + \Gamma^2} \quad (17)$$

and approximately [for $|(\omega - \omega_d)Z| \ll \Gamma$] (Ref. 22)

$$\frac{N(\omega)}{N_0} = \frac{2\Gamma}{\pi} \ln \left| \frac{W_C}{\Gamma} \right| + \frac{(\omega - \omega_d)^2 Z^2}{\pi \Gamma}, \quad (18)$$

where the first term is the value right at $\omega = \omega_d$ and the ω variation off the Dirac point is quadratic in $\omega - \omega_d$. Note that $N(\omega_d) \rightarrow 0$ as $\Gamma \rightarrow 0$ in Eq. (18). Also from Eq. (17), as $\Gamma \rightarrow 0$, $A(\pm \epsilon, \omega) \sim \delta[(\omega - \omega_d)Z \pm \epsilon]$ which gives for $\mu_0 < \omega_E$ a linear variation in $N(\omega)$ out of ω_d with slope modified by Z . We have tested these analytic results against numerical work and offer a comparison in the bottom frame of Fig. 6. The

dashed red curve fits very well the solid blue curve in the region of the Dirac point. To end this section, we comment on the range of validity of the approximate but very useful Eqs. (10) and (15) for renormalized chemical potential and Dirac point position, respectively. In Fig. 7, we compare exact results for μ (solid red curve) and ω_d (long-dashed blue curve) with the approximation, Eqs. (10) and (15), respectively [i.e., $\mu_0/(1 + \lambda^{\text{eff}})$, short-black curve]. At small μ_0 , the agreement is excellent as we expected. The deviations at higher values of $\mu_0 \gtrsim 350$ meV should be noted and could be of importance in some applications. Finally note that on the scale shown, μ and $|\omega_d|$ track each other well.

III. MORE REALISTIC PHONON SPECTRA

In a metal with constant density of states in the important energy range for phonons, the electron-phonon interaction

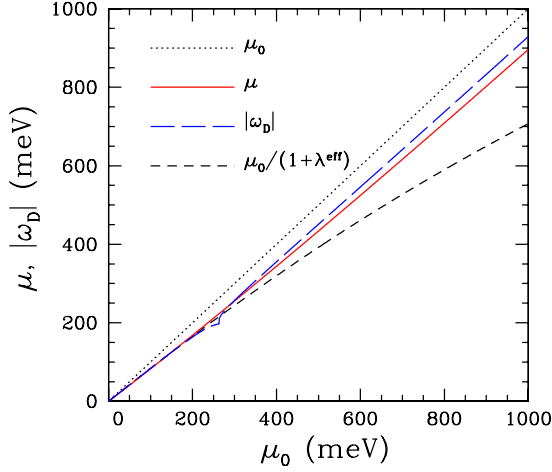


FIG. 7. (Color online) Comparison of μ (red solid curve) and $|\omega_D|$ (long-dashed blue curve) with approximate relation $\mu_0/(1+\lambda^{\text{eff}})$ (short-dashed black curve) as a function of μ_0 . The dotted line is for comparison and gives μ_0 unrenormalized.

does not renormalize its value.²² The essential argument can be seen from Eq. (1) which is to be integrated over energy but $\int_{-\infty}^{+\infty} N(0) d\epsilon A(\epsilon, \omega) = N(0)$ independent of ω . This means that phonons will not show up in normal density-of-states spectroscopy. But in graphene, this no longer holds for two reasons. First, the Dirac density of states is linear in ϵ rather than constant as can be seen in Eq. (3) and after integration Σ remains in the formula. Second, we have finite bands and it has been noticed by Knigavko *et al.*⁴⁶ that this also provides a mechanism whereby an image of the phonon structure appears in the electronic density of states. To examine phonon structure it is convenient to move away from coupling to a single Einstein phonon as we have done so far in Eq. (2) for the self-energy. For a distribution of phonon energies $P(\nu)$, it is necessary to average Eq. (2) over the desired distribution. As a model, we use the truncated Lorentzian form of Ref. 13

$$P(\nu) = \frac{A'}{\pi} \left[\frac{\delta}{(\nu - \omega_0)^2 + \delta^2} - \frac{\delta}{\delta_c^2 + \delta^2} \right] \theta(\delta_c - |\omega_0 - \nu|), \quad (19)$$

where it is peaked at ω_0 with width δ and truncated at energy $\omega_0 \pm \delta_c$. A' is adjusted to give λ used previously. With this distribution

$$\Sigma_{\text{lor}}(\omega) = \int_{-\infty}^{\infty} P(\nu) \Sigma(\omega, \nu) d\nu, \quad (20)$$

where $\Sigma(\omega, \nu) \equiv \Sigma(\omega)$ of Eq. (2) and ω_E of that equation now becomes a variable ν . Also, the A of Eq. (2) is omitted in favor of Eq. (19) which enters into Eq. (20). $\Sigma_{\text{lor}}(\omega)$ is then used for the self-energy in the DOS calculation using Eq. (3). In our calculations, we have used $\omega_0 = 200$ meV, $\delta = 15$ meV, and $\delta_c = 30$ meV.

To see better the phonon structures encoded in the electronic density of states $N(\omega)$ of Figs. 1 and 3, it is convenient to take a first derivative. This is shown in Fig. 8 for several cases. $d[N(\omega)/N_0]/d\omega$ is normalized such that in the bare

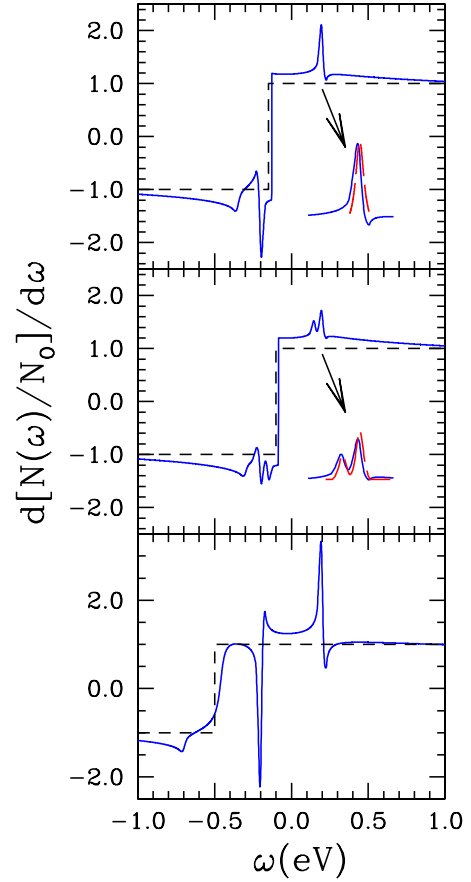


FIG. 8. (Color online) Derivative of the electronic density of states. Dashed black line is the bare case and the solid blue curve includes phonons. The top frame is for a bare chemical potential $\mu_0 = 150$ meV and coupling to a Lorentzian phonon distribution peaked at $\omega_0 = 200$ meV while the middle is the same but a distribution with two Lorentzian peaks and $\mu_0 = 100$ meV. The insets indicated by an arrow, show the structure of the solid blue curve in comparison with the input electron-phonon spectral function (red dashed curve). See text for further discussion. The lower frame is also for the Lorentzian distribution used for the upper frame but now $\mu_0 = 500$ meV.

band, it is one at energies above the Dirac point and minus one below, with a jump at that point. This is represented in Fig. 8 as the black dashed curves with $\mu_0 = 150$ meV for the top and middle frames and $\mu_0 = 500$ meV in the bottom frame. The solid blue line contains the phonons. In the top frame, we see a prominent phonon structure at $\omega = \pm \omega_0$ in $d[N(\omega)/N_0]/d\omega$ which is superimposed on the bare-band background above which it rises by more than a factor of two. On the negative-energy side there is a further smaller structure at $(-\mu_0 - \omega_0)$. All three phonon structures can be traced to logarithmic singularities in the self-energy of Eq. (5) of the form $\ln|\omega \pm \omega_0|$ for the first two and $(\omega + \mu_0 + \omega_0) \ln|\omega + \mu_0 + \omega_0|$ for the last which is a weaker singularity. Note that the vertical drop in the solid curve is not at $\omega = -\mu_0$ but is rather shifted to the right because the Dirac point has been shifted and this drop signals the position of ω_d rather than of $-\mu_0$. The value of this derivative at $\omega = 0$ has height equal to $(1 + \lambda^{\text{eff}})$ and this can be used to measure this

renormalization parameter. Of course this is only possible if one knows the value of the bare-band Fermi velocity v_0 . Additional renormalizations such as Coulomb interactions⁴⁷ are not treated here.

On the scale of this figure, it is clear that the phonon structure should be easily detectable. In the inset indicated by the solid arrow, we compare the structure in the first derivative of the DOS (blue solid curve) with the input spectral density (red dashed curve) scaled down by a factor of 10. Except for a small shift between the two curves, there is excellent agreement and conclude that the first derivative not only indicates where the boson structure lies but also captures well the correct profile of the Lorentzian spectra that we have used. This is further emphasized in the middle frame where two Lorentzians at slightly different energies $\omega_{01}=150$ meV and $\omega_{02}=200$ meV are used with the second peak height chosen to be twice that of the first. Again the reproduction of the details of the input electron-phonon spectral density, which is scaled down by a factor of 10, is excellent. This demonstrates that normal density-of-states spectroscopy can potentially be used to probe the phonon structures in graphene. The technique could also be extended to other structures such as those due to hole-particle excitations and plasmons. The lower frame is the same as the top frame but now $\mu_0=500$ meV beyond the phonon energies of ~ 200 meV in our model. In this case the phonon structures are even bigger as we expect since the electron-phonon interaction reflects the bare density of states which increases with increasing energy. This expected increase in coupling can clearly be probed in density-of-states measurements. A feature to be noted is that because $\mu_0 > \omega_0$ in this frame, the Dirac point is changed to the quadratic behavior shown in the lower frame of Fig. 6 and this leads to a drop in $dN(\omega)/d\omega$ which is no longer vertical but instead is smeared. Finally, we note that while the first derivative already gives a rather good image of the shape of the underlying electron-phonon spectral function, a formal inversion of Eq. (3) along the lines used in superconductivity by McMillan and Rowell⁴⁸ could be used to get its size and shape for each doping value.

As we noted with reference to the top frame of Fig. 1, the logarithmic singularities at $\omega = \pm \omega_E$ in Eq. (5) for $\text{Re } \Sigma(\omega)$ no longer appear when the chemical potential $\mu_0=0$ and the bands are filled exactly to the Dirac point. This is shown in Fig. 9 (top frame). Only a small kink (i.e., change in slope) remains at $\omega = \pm \omega_E$. This fact has important consequences for experiment. While the density of states as a function of ω still knows about the renormalization factor of $1+\lambda^{\text{eff}}$ (middle frame) there is no additional logarithmic-type signature of the Einstein phonon mode. Consequently, compared with the examples of Fig. 8, only very small peaks are seen at $\omega = \pm \omega_E$ in the derivative, as shown in Fig. 9 (bottom frame). Nevertheless, one can see the $1+\lambda^{\text{eff}}$ renormalization at low frequency in this frame, given as the magnitude of the height of the curve near zero frequency. In their STM results, Li *et al.*²³ find structure in the DOS at 155 meV. In addition, they find a renormalization which they determine to be $\lambda^{\text{eff}}=0.26$, for a case of doping very close to the charge neutrality point. This case was addressed in our previous short communication²² which was aimed toward a detailed evalu-

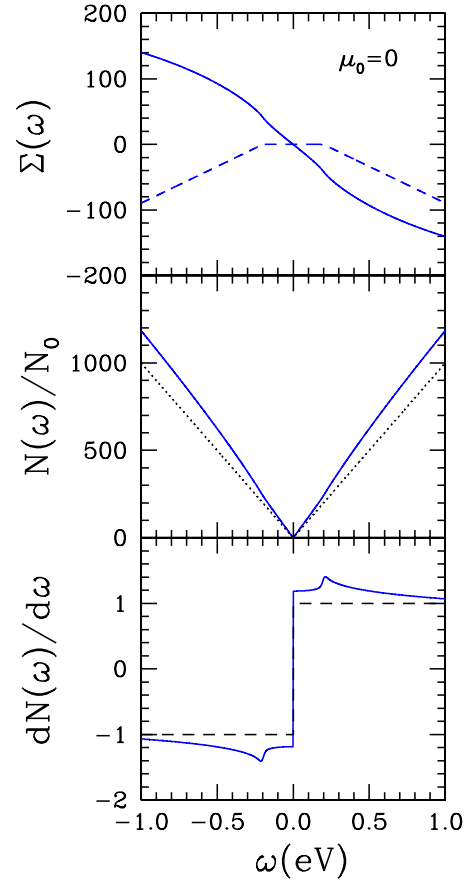


FIG. 9. (Color online) Top frame: self-energy $\Sigma(\omega)$ for $\mu_0=0$ in units of meV for the real (solid curve) and imaginary part (dashed curve). The density of states for this case is shown in the middle frame in units of meV with the bare DOS given as the dotted curve. Derivative of the DOS normalized to N_0 is shown in the bottom frame with the dashed black line is the bare case. In all cases, the solid blue curves includes phonons.

ation of the data analysis procedure used by Li *et al.* for extracting a value of the mass enhancement. From that we conclude that the data may support a larger value of λ^{eff} , possibly as large as 0.4. Including Coulomb interactions⁴⁷ may change these estimates somewhat.

IV. ARPES

The charge-carrier spectral density $A(\mathbf{k}, \omega)$ given by Eq. (1) can be measured in ARPES experiments. The technique is directional and measures $A(\mathbf{k}, \omega)$ as a function of ω for any direction and magnitude of momentum \mathbf{k} . Here, because of the symmetry only $\epsilon = \pm \hbar v_0 |\mathbf{k}|$ enters. As we have already noted, if the imaginary part of the electron-phonon self-energy is infinitesimal, $A(\pm \epsilon, \omega)$ would reduce to a delta function and provide the dressed energy E_k corresponding to the bare ϵ_k through the equation $E_k - \text{Re } \Sigma(E_k) + \mu - \epsilon_k = 0$. In Fig. 10, we show results for E_k in the case of $\mu_0 = 400$ meV. The dashed black lines are the bare dispersions and the solid blue curves are the renormalized energies. Several features of this figure need to be noted. The renormalized dispersions show a clear “kink” at the peak phonon

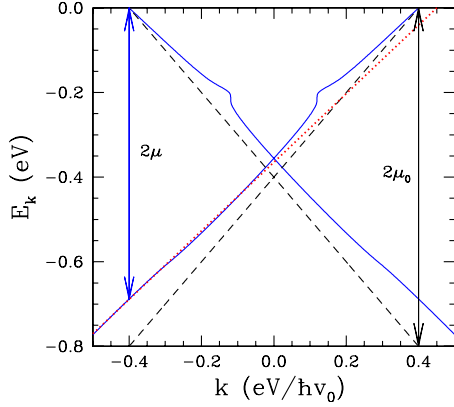


FIG. 10. (Color online) Renormalized energies (solid blue curves) E_k as a function of k in units of $\text{eV}/(\hbar v_0)$ for a case with $\mu_0=400$ meV. Twice the bare and dressed chemical potential are indicated by vertical arrows, long and short, respectively. The bare curves are shown as dashed black lines and the dotted is a line chosen to fit the dressed curve asymptotically at large negative energy.

energy $\omega_0=200$ meV. In the calculations, we used our Lorentzian model for the distribution of phonon energies about ω_0 otherwise the kink would actually show a logarithmic singularity. For a simple metal with a constant DOS around the Fermi energy, the same phonon anomaly would arise but at higher energies (below the Fermi energy) the renormalized curve would rapidly return to the bare value as the real part of $\Sigma(\omega)$ drops to zero. This is not true for graphene because the density of electron states increases linearly with increasing energy and this means that $|\text{Re } \Sigma(\omega)|$ increases as we saw in the top frame of Fig. 1. The phonon structures are superimposed on this more gradual increase in $|\text{Re } \Sigma(\omega)|$ versus ω . The dotted red line in Fig. 10 brings out this feature clearly. It has been drawn to match the dressed dispersions at large negative energies. In contrast to what would be the case for the bare dispersions, this asymptotic line when extended toward the Fermi energy does not cross through the Fermi energy. This has been noted in the ARPES data of Bostwick *et al.*²⁵ In our calculations this is a direct consequence of the fact that the electron-phonon renormalizations continue to increase at high energies because of the continuing increase in the bare density of states. In the actual experimental data, other renormalizations would also contribute. While the slope of the bare dispersion curves (dashed black lines) gives directly the bare velocity v_0 the slope of the asymptotic dotted line is smaller and would give a smaller value of the effective velocity of light for graphene should it be used to define the bare bands. It is close but not the same as the renormalized effective velocity of light $v_0/(1+\lambda^{\text{eff}})$. The vertical arrows in Fig. 10 identify renormalized (shorter blue arrow) and bare (longer black arrow) chemical potentials, respectively. It is clear that μ is about 15% smaller. This is close but does not quite correspond to the factor of $1+\lambda^{\text{eff}}=1.19$ in our calculations indicated in Eq. (10) which is strictly valid only for $\mu_0 \ll \omega_0$. Nevertheless, the differences are small. Here the factor of 1.19 gives exactly the slope of E_k out of the Fermi energy.

Of course, the imaginary part of $\Sigma(\omega)$ in Eq. (1) for $\omega \neq 0$ would never be zero and we would not have perfectly

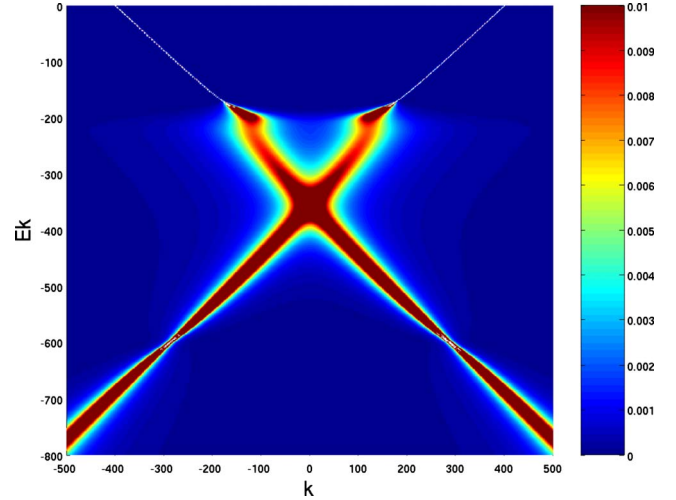


FIG. 11. (Color online) Color map of interacting dispersions E_k in units of meV as a function of k in units of $\text{meV}/(\hbar v_0)$. The bare chemical potential $\mu_0=400$ meV and a Lorentzian phonon spectrum with $\omega_0=200$ meV were used.

well-defined dressed dispersion curves. In such a circumstance, it is useful to use a color map to show the constant energy contours of $A(\epsilon, \omega)$. This is done in Fig. 11. Cuts at different values correspond to different colors as indicated on the scale shown on the right (units of meV^{-1}). Because we have used a phonon spectrum which starts at $\omega=170$ meV for this figure ($\omega_0-\delta_c$), there is no quasiparticle lifetime above -170 meV. Below this energy the curves widen and reflect the broadening. We see clearly the peak of the phonon anomaly at -200 meV but the identification of the position of the Dirac point becomes somewhat ambiguous because of the broadening of the curves. The renormalized $|\mu|=344$ meV for this case and according to Fig. 7 this almost coincides with $|\omega_d|$. The pinching at -600 meV is due to the small value of the imaginary part of the self-energy at $-\mu_0-\omega_0$ as we have already seen in the middle frame of Fig. 1 for a different value of chemical potential. Other interactions such as electron-hole-particle pair formation or coupling due to plasmons are expected to lift this pinching and provide a finite lifetime. It is clear from this figure that the constructions used in Fig. 10 to identify the dotted asymptotic line as well as the interacting chemical potential are not as well defined when broadening is included in the theory.

V. ELECTRON-PHONON INTERACTION ON dc CONDUCTIVITY

Next we turn to the optical conductivity. In units of the universal background conductivity $\sigma_0=\pi e^2/2h$, where e is the electron charge and h is Planck's constant, the real part of the frequency-dependent conductivity $\sigma(T, \Omega)$ at frequency Ω and temperature T is given by

$$\frac{\sigma(T, \Omega)}{\sigma_0} = \frac{4}{\Omega} \int_{-\infty}^{\infty} d\omega [f(\omega) - f(\omega + \Omega)] \int_0^{W_C} \epsilon d\epsilon [A(\epsilon, \omega) + A(-\epsilon, \omega)] [A(\epsilon, \omega + \Omega) + A(-\epsilon, \omega + \Omega)], \quad (21)$$

where we have ignored vertex corrections. In metal physics,

this can be incorporated approximately by an extra weighting of $(1 - \cos \theta)$ in the calculation of the scattering rate changing it from a quasiparticle to transport rate.¹⁰ This has recently been verified to hold as well for the specific case of the dc conductivity of graphene by Cappelluti and Benfatto.⁴⁹ The function $f(\omega) = 1/[\exp(\beta\omega) + 1]$ is the Fermi occupation factor with β as the inverse temperature. We start with a general observation that

$$\sigma_{\mu < 0}(T, \Omega) = \sigma_{|\mu|}(T, \Omega). \quad (22)$$

To establish this symmetry, we note first that for negative values of the chemical potential μ , the carrier spectral function satisfies

$$A_{\mu < 0}(\epsilon, \omega) = A_{|\mu|}(-\epsilon, -\omega), \quad (23)$$

where we have used the symmetries given with Eqs. (5) and (6). Also, Eq. (21) can be rewritten as

$$\begin{aligned} \frac{\sigma_{\mu < 0}(T, \Omega)}{\sigma_0} &= \frac{4}{\Omega} \int_{-\infty}^{\infty} d\omega [f(\omega) - f(\omega + \Omega)] \int_0^{W_C} \epsilon d\epsilon [A(\epsilon, -\omega) \\ &+ A(-\epsilon, -\omega)] [A(\epsilon, -\omega - \Omega) \\ &+ A(-\epsilon, -\omega - \Omega)]. \end{aligned} \quad (24)$$

Noting Eq. (23), then Eq. (22) follows.

Taking $\Omega=0$ in Eq. (21) gives the dc conductivity at finite T

$$\begin{aligned} \frac{\sigma_{dc}(T)}{\sigma_0} &= -4 \int_{-\infty}^{\infty} d\omega \frac{\partial f(\omega)}{\partial \omega} \int_0^{W_C} \epsilon d\epsilon [A^2(\epsilon, \omega) + A^2(-\epsilon, \omega) \\ &+ 2A(\epsilon, \omega)A(-\epsilon, \omega)]. \end{aligned} \quad (25)$$

We have verified numerically that in Eq. (25), we can send W_C to infinity within good approximation. This simplifies the result and we get

$$\begin{aligned} \frac{\sigma_{dc}(T)}{\sigma_0} &= -\frac{4}{\pi^2} \int_{-\infty}^{\infty} d\omega \frac{\partial f(\omega)}{\partial \omega} \left\{ 1 + \left[\frac{a(\omega)}{\Gamma(\omega)} + \frac{\Gamma(\omega)}{a(\omega)} \right] \right. \\ &\times \left. \tan^{-1} \left[\frac{a(\omega)}{\Gamma(\omega)} \right] \right\} \end{aligned} \quad (26)$$

with $\Gamma(\omega) = -\text{Im} \Sigma(\omega)$ and $a(\omega) = \omega - \text{Re} \Sigma(\omega) + \mu$. Note that for $\Sigma(\omega)$, we have neglected the temperature dependence that would enter Eq. (2) at finite temperature¹³ and hence our results here are for low T . At zero temperature $-\partial f(\omega)/\partial \omega$ in Eq. (26) becomes a Dirac delta function centered around $\omega = 0$ (i.e., $\delta(\omega)$) and

$$\begin{aligned} \frac{\sigma_{dc}(T=0)}{\sigma_0} &= \frac{4}{\pi^2} \left\{ 1 + \left[\frac{\mu - \text{Re} \Sigma(\omega=0)}{\Gamma(\omega=0)} \right] \right. \\ &+ \left. \frac{\Gamma(\omega=0)}{\mu - \text{Re} \Sigma(\omega=0)} \right\} \tan^{-1} \left[\frac{\mu - \text{Re} \Sigma(\omega=0)}{\Gamma(\omega=0)} \right]. \end{aligned} \quad (27)$$

But $\mu - \text{Re} \Sigma(\omega=0)$ in Eq. (27) can be replaced by μ_0 , the bare-band chemical potential from Eq. (7). Also, at $\omega=0$ and $T=0$, the electron-phonon interaction does not contribute to the scattering rate which therefore reduces to the residual

scattering rate η , i.e., $\Gamma(\omega=0) \equiv \eta$, which is small but finite for graphene. Thus, the electron-phonon interaction has entirely dropped out of Eq. (27), which reduces to its bare-band value. This means that the familiar result^{10,11} that the electron-phonon interaction does not change the dc conductivity of ordinary metals also holds for graphene.

For $\mu - \text{Re} \Sigma(\omega=0) \equiv \mu_0 \ll \eta$ in Eq. (27), we get the universal dc limit,^{50,51} unrenormalized by the electron-phonon interaction

$$\sigma_{dc}(T=0) = \frac{8}{\pi^2} \sigma_0 = \frac{4e^2}{\pi h} \quad (28)$$

which differs from the universal ac background value σ_0 by a factor of $8/\pi^2 \approx 0.81$. The first correction for finite μ_0 is included when Eq. (28) is multiplied by $[1 + (\mu_0/\eta)^2/2]$. In the opposite limit of $\mu - \text{Re} \Sigma(\omega=0) \gg \eta$, we get instead

$$\sigma_{dc}(T=0) = \frac{e^2}{h} \frac{2[\mu - \text{Re} \Sigma(\omega=0)]}{2\eta} = \frac{e^2}{h} \frac{2\mu_0}{2\eta}. \quad (29)$$

Here, $2\mu_0$ is the optical spectral weight removed from the universal background at finite chemical potential (in the bare band) which reappears as a Drude-type contribution about $\Omega=0$. Note that $1/\tau = 2\eta$ is the transport scattering rate. In this limit, the dc conductivity is no longer universal, i.e., η does not drop out as it did in Eq. (28), however the electron-phonon interaction has dropped out. This is similar to the well-known result^{10,11} in conventional metals, that the electron-phonon interaction does not change the value of the dc conductivity. This remains true for graphene at $T=0$, and can be traced to Eq. (27). $\sigma_{dc}(T=0)$ does not depend on the electron-phonon interaction because of the appearance of the chemical-potential shift factor $\text{Re} \Sigma(\omega=0)$, which changes μ to μ_0 , the bare-band value, and $\Gamma(\omega=0)$ reduces to the residual scattering rate.

Returning to Eq. (25), it is useful to separate intraband and interband contributions. The first two terms are intraband because they involve transitions within the same Dirac cone while the last term involves transitions between lower and upper cones. In a conventional metal only the intraband contribution arises in discussions of the dc conductivity. In Fig. 12, we show results for $\sigma_{dc}(T=0)$ in units of σ_0 as a function of $[\mu - \text{Re} \Sigma(\omega=0)]/\eta \equiv \mu_0/\eta$. The solid (red) curve is the interband piece, the long-dashed (blue) curve is the intraband, and the short dashed (black) is the sum. Both the intraband and interband transitions contribute equally to the universal dc value which corresponds to $[\mu - \text{Re} \Sigma(\omega=0)]/\eta = \mu_0/\eta = 0$, i.e., the lower cone is filled to the Dirac point and the upper cone is empty. As μ_0 is increased and the material is doped away from the neutrality point, the interband contribution decreases while at the same time the sum increases rather substantially. What determines the scale of this increase is the value of the ratio of the chemical potential to the residual scattering rate η . While the value of η is somewhat uncertain for graphene and will vary with sample quality, it is expected to be small and of order of 1.0 meV so that the value of the dc conductivity can be increased a lot for easily attained values of the chemical potential, say μ_0 of order a few hundred meV.

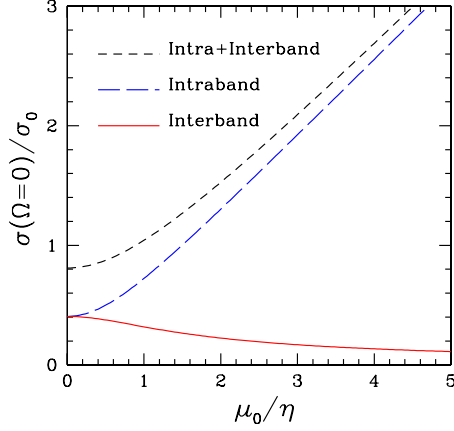


FIG. 12. (Color online) dc conductivity $\sigma(\Omega=0)$ at $T=0$ in units of the universal background value $\sigma_0 = \pi e^2/2h$. The solid red curve gives the interband contribution, the long-dashed blue curve, the intraband and the short-dashed black curve, the sum as a function of $[\mu - \text{Re } \Sigma(\omega=0)]/\eta \equiv \mu_0/\eta$, with μ as the chemical potential, μ_0 as its bare-band value, $\text{Re } \Sigma(\omega=0)$ as its shift, and η as the residual quasiparticle scattering rate.

Returning to Eq. (26) which gives the dc conductivity at finite temperature T , we note that the value of $\text{Re } \Sigma(\omega)$ for finite ω now enters the formula even for $\mu=0$ (Dirac point is at the Fermi surface) and consequently the dc conductivity is affected by the electron-phonon interaction. It is only for $T=0$, $\mu_0=0$ that we get $\sigma_{dc} = 0.81\sigma_0$ independent of electron-phonon renormalization.

In a conventional metal, if only impurity (elastic) scattering is accounted for, the dc conductivity does not change with increasing temperature. To get a change it is necessary to include inelastic processes. This is not so for graphene. Including only residual scattering and no electron-phonon renormalization, the formula for the dc conductivity Eq. (26) reduces to

$$\frac{\sigma_{dc}(T)}{\sigma_0} = \frac{4}{\pi^2} \int_{-\infty}^{\infty} \frac{dx}{4 \cosh^2[(x - \tilde{\mu})/2]} \times \left[1 + \left(\frac{x}{\tilde{\eta}} + \frac{\tilde{\eta}}{x} \right) \tan^{-1} \left(\frac{x}{\tilde{\eta}} \right) \right]. \quad (30)$$

In Fig. 13, we show on a logarithmic scale $\sigma(\Omega=0, T)/\sigma_0$ as a function of $\tilde{\mu} \equiv \mu/T$ for various values of $\tilde{\eta} \equiv \eta/T$. Here, $\mu = \mu_0$, the bare-band chemical potential, as $\Sigma(\omega)$ has been taken to be zero. We first note that at $\tilde{\mu}=0$, the universal limit is no longer universal unless the temperature is much smaller than the residual quasiparticle scattering rate η . An analytic expression valid for $T/\eta \ll 1$ is⁵²

$$\sigma_{dc}(T) = \frac{4e^2}{\pi h} \left[1 + \frac{\pi^2}{9} \left(\frac{T}{\eta} \right)^2 \right]. \quad (31)$$

For $\eta=T$, the dc conductivity has increased by more than a factor of two over its $T=0$ value. It is clear that in clean systems, it is necessary to go to very low temperatures in order to observe the universal limit. It is also clear that the chemical potential is to be small compared with η . It is the

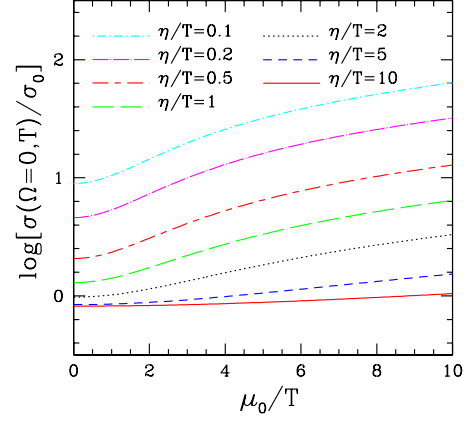


FIG. 13. (Color online) The dc conductivity $\sigma(\Omega=0, T)$ at finite, but small, temperature T in units of $\sigma_0 = \pi e^2/2h$ as a function of μ_0/T for several values of η/T with μ_0 , the bare chemical potential and η , the residual quasiparticle scattering rate. Here, for simplicity, phonon renormalizations are taken to be zero.

residual scattering rate which sets the scale on T and μ . The conditions to observe the universal limit are $T \ll \eta$ and $\mu \ll \eta$. We turn next to finite Ω in the microwave or Terahertz region where Ω is of order η , and study the evolution of the conductivity from its dc value to its universal ac background value.

VI. LOW-FREQUENCY CONDUCTIVITY

In Fig. 14, we show results for $\sigma(\Omega)$ at $T=0$ in the frequency region spanning a few times the energy of the quasiparticle scattering rate η . The top left-hand frame shows $\sigma(\Omega)/\sigma_0$ versus Ω up to 100 meV for zero chemical poten-

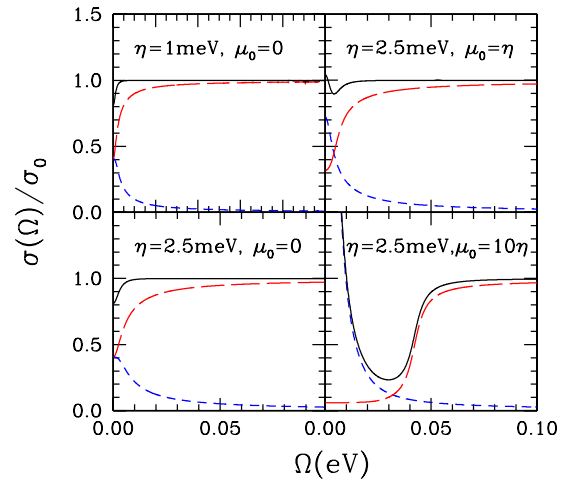


FIG. 14. (Color online) The conductivity $\sigma(\Omega)$ at $T=0$ in units of $\sigma_0 = \pi e^2/2h$ as a function of Ω emphasizing the low-frequency region. Left frames are for zero chemical potential ($\mu_0=0$) and quasiparticle residual scattering rate $\eta=1.0$ and 2.5 meV. Right frames are for $\eta=2.5$ meV with $\mu_0=\eta$ and 10η . Long-dashed red curve is the interband contribution, short-dashed blue is the intraband, and solid black is the sum. Electron-phonon renormalizations are included using the parameters previously discussed.

tial with $\eta=1$ meV while the lower frame is the same but now $\eta=2.5$ meV. In both cases the long-dashed (red) curve is the interband contribution and the short-dashed (blue) is the intraband. The sum is the solid black curve. We see that at $\Omega=0$, the universal limit is reached for both values of η as expected. As Ω is increased $\sigma(\Omega)$ increases toward the universal background value $\sigma_0=\pi e^2/(2h)$. The energy scale on which saturation is reached is set by the value of η and hence will vary with sample quality. The two right-hand panels are similar but are for finite chemical potential, with $\mu_0=\eta$ for the top and $\mu_0=5\eta$ for the bottom, and $\eta=2.5$ meV in both cases. It is clear that the conductivity in the low Ω region is greatly affected by finite μ_0 and is nonuniversal. This arises because at finite μ_0 , the interband transitions below $2\mu_0$ are Pauli blocked and the optical spectral weight involved is transferred to the intraband transitions. This provides a Drude peak with finite effective plasma frequency proportional to $2\mu_0$. In the top right panel of Fig. 14, $\mu_0=\eta$ so that we are not in the universal dc limit regime and its value is in fact already larger than the universal background value σ_0 . As Ω is increased, $\sigma(\Omega)/\sigma_0$ drops, shows a minimum before rising again to reach its universal background value. The energy scale for this final rise to saturation remains η as in the left-hand panels but this is because η is of order μ_0 . For a case $\mu_0>\eta$ as in the lower right panel, specifically with $\mu_0=10\eta$, the Drude at small Ω is much more pronounced as compared with the upper frame and it is now $2\mu_0$ which sets the energy scale for recovery of the conductivity to its universal background value. An interesting feature of the interband contribution to the conductivity (long-dashed red curve) in this case is the long tail extending to $\Omega=0$ which is nearly constant before its main rise around $\Omega=2\mu_0$. This behavior can be understood analytically as we now show.

At zero temperature, for small but finite Ω the conductivity is given approximately by

$$\frac{\sigma(\Omega)}{\sigma_0} = \frac{4}{\Omega} \int_{-\Omega}^0 d\omega \sum_{\pm} \int_0^{\infty} \frac{\epsilon d\epsilon}{\pi^2} \left[\frac{\eta}{[\omega(1+\lambda_{\text{eff}}) \pm \epsilon + \mu_0]^2 + \eta^2} \right] \times \left[\frac{\eta}{[(\omega+\Omega)(1+\lambda_{\text{eff}}) \pm \epsilon + \mu_0]^2 + \eta^2} \right], \quad (32)$$

where we have noted the ω is also small and have used $-\lambda_{\text{eff}}\omega$ for $\text{Re } \Sigma(\omega)$, after subtraction of the constant piece $\Sigma(\omega=0)$. The imaginary part of the self-energy due to phonons is zero so that only the residual contribution remains. Should the acoustic phonons have been included in the model, $\text{Im } \Sigma(\omega)$ would be finite, but this effect is small in graphene and neglected here. The sum over \pm leads to four terms in Eq. (32), two intraband contributions (same sign) and two interband (opposite signs of ϵ in pair of terms). The integral over energy can be performed analytically and the sum over $+$ and $-$, i.e., upper and lower Dirac cone performed. Starting first with the intraband piece and writing $\bar{\Omega} \equiv \Omega(1+\lambda_{\text{eff}})$ and $\bar{\omega} \equiv \omega(1+\lambda_{\text{eff}})$, we get

$$\frac{\sigma_{\text{intra}}(\Omega)}{\sigma_0} = \frac{4\eta^2}{\pi^2\Omega} \int_{-\Omega}^0 d\omega \left\{ \frac{-2}{\bar{\Omega}} \frac{1}{4\eta^2 + \bar{\Omega}^2} \left[\left(\bar{\omega} + \frac{\bar{\Omega}}{2} \right) + \mu_0 \right] \times \ln \left| \frac{[\bar{\omega} + \mu_0]^2 + \eta^2}{[(\bar{\omega} + \bar{\Omega}) + \mu_0]^2 + \eta^2} \right| \right\} - 4\eta - \frac{\bar{\Omega}}{\eta} [(\bar{\omega} + \bar{\Omega}) + \mu_0] \tan^{-1} \left(\frac{(\bar{\omega} + \bar{\Omega})}{\eta} + \mu_0 \right) + \frac{\bar{\Omega}}{\eta} (\bar{\omega} + \mu_0) \tan^{-1} \left(\frac{\bar{\omega}}{\eta} + \mu_0 \right). \quad (33)$$

Assuming $\omega, \Omega, \eta \ll \mu_0$, expression (33) greatly reduces and we get

$$\frac{\sigma_{\text{intra}}(\Omega)}{\sigma_0} = \frac{4|\mu_0|}{\pi} \frac{2\eta}{\Omega^2(1+\lambda_{\text{eff}})^2 + 4\eta^2} \quad (34)$$

for the intraband contribution to the conductivity when $\Omega \ll \mu_0$, as well as, $\eta \ll \mu_0$. The form, Eq. (34), is a Drude with effective optical scattering rate $2\eta/(1+\lambda_{\text{eff}})$ and effective plasma frequency of $4\mu_0/[\pi(1+\lambda_{\text{eff}})]$. While we have made approximations to derive Eq. (34), we have verified in numerical work for Fig. 14 right bottom frame that the long-dashed blue curve follows Eq. (34) very well. The result Eq. (34) is the same as found in conventional metals. The coherent part of the conductivity is a Drude form with scattering rate and plasma frequency renormalized by $(1+\lambda_{\text{eff}})$ and the dc limit remains unrenormalized by λ_{eff} . Here for simplicity, we have used a constant residual scattering rate. For graphene, this scattering rate can itself be frequency dependent and this can change the Drude line shape which then reflects this additional energy dependence as described in Ref. 35.

Application of the same sort of algebra for the interband contribution to the conductivity in the limit Ω and $\eta \ll \mu_0$, gives a leading contribution which is *frequency independent*

$$\frac{\sigma_{\text{inter}}(\Omega)}{\sigma_0} = \frac{1}{\pi} \frac{2\mu_0\eta}{\eta^2 + \mu_0^2} \quad (35)$$

($\Omega < \omega_E$) and in sharp contrast to Eq. (34) is independent of the electron-phonon-renormalization parameter λ_{eff} . Thus, while the intraband Drude contribution is renormalized by the electron-phonon interaction in the same way as in ordinary metals, the interband is not. Equally remarkable is that Eq. (35), in contrast to Eq. (34), is independent of photon energy, as we already noted in the lower right-hand frame of Fig. 14 where we present numerical results. The interband contribution (long-dashed red curve) remains essentially constant at its dc value even for $\Omega \approx 2\mu_0$ at which point it begins a steep rise and eventually makes the major contribution to the universal background value. At small Ω it is the reverse that holds, the interband piece is small while the intraband Drude-type contribution is dominant. Additional results for the interband contribution to the conductivity for photon energies less than and slightly above the value of twice the chemical potential are shown in Fig. 15. Here we span values of μ_0 from zero to ten times η , as labeled on the

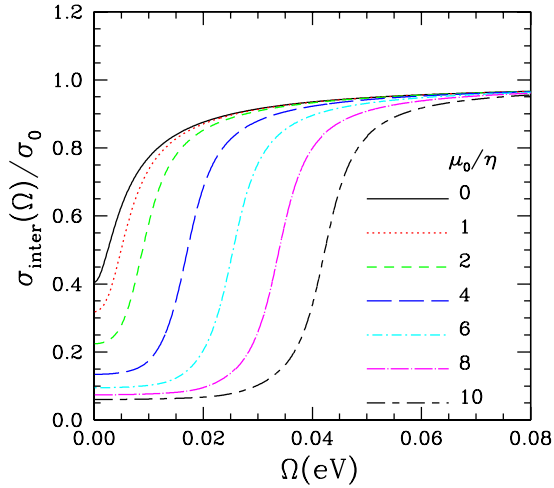


FIG. 15. (Color online) The interband conductivity $\sigma_{inter}(\Omega)$ at $T=0$ in units of $\sigma_0=\pi e^2/2h$ as a function of photon energy Ω emphasizing the low-frequency region, for varying values of μ_0/η , with $\eta=2.5$ meV. Electron-phonon renormalizations are included as described previously.

figure. Only the first curve (solid black) satisfies the condition for the universal dc limit and in this case, the curve starts at a value of $4/\pi^2 \sim 0.4$ and makes half the contribution to the universal dc conductivity. Furthermore, it rapidly rises to its universal ac background value on the scale of 2η , with $\eta=2.5$ meV. All other curves start with $\sigma(\Omega)/\sigma_0$ below $4/\pi^2$ at $\Omega=0$. This is true even for the red dotted curve for which $\mu_0=\eta$. The last few conform well to the analytic prediction of Eq. (35) that $\sigma_{inter}(\Omega)/\sigma_0=(2\mu_0/\pi\eta)/[1+(\mu_0/\eta)^2]$, which we see extends to $\Omega \leq 2\mu$ and, as noted before, the main rise toward the universal background value is set by 2μ rather than by η . The few intermediate curves show the evolution from one regime to the other.

VII. INFRARED CONDUCTIVITY

So far we have examined the small photon energy range of the ac conductivity as compared with the value of the phonon energy $\omega_E=200$ meV in our model. In Fig. 16, we show results to $\Omega=1$ eV for $\mu_0=150$ meV (top frame) and $\mu_0=400$ meV (bottom frame). The dashed red curve, which is included for comparison, give results without the electron-phonon interaction (bare-band case) but with a phenomenological impurity transport scattering rate of 2η with $\eta=2.5$ meV (constant). The solid blue curve has phonons. The first thing to note when comparing these curves is that the main rise in $\sigma(\Omega)/\sigma_0$, indicating the increase in interband transitions, occurs at twice the value of the dressed chemical potential in the solid curve while it occurs at $2\mu_0$ for the bare bands. This translates into a considerable shift downward of this prominent threshold for absorption. This is easily understood with the help of Fig. 10 where bare band and renormalized dispersion curves are shown. Absorption of light for the interband case proceeds through vertical transitions from an occupied state in the lower Dirac cone to an unoccupied state in the upper Dirac cone since the photon transfers no

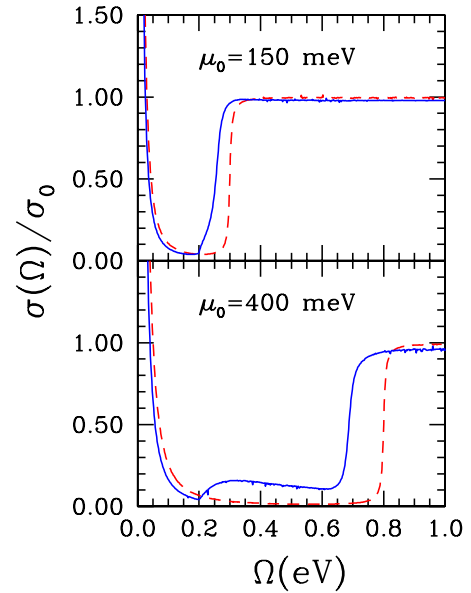


FIG. 16. (Color online) ac conductivity $\sigma(\Omega)/\sigma_0$ for two values of chemical potential $\mu_0=150$ meV (top frame) and $\mu_0=400$ meV (bottom frame), one below and one above the phonon energy of $\omega_E=200$ meV. The dashed red curve was obtained without electron-phonon renormalization and the solid blue is with.

momentum to the electronic system. This is shown as the arrows which applies to the lowest energy transition allowed by the Pauli exclusion principle, which blocks transitions below this energy. For the bare clean bands this energy is just $2\mu_0$ (large black arrow), twice the bare chemical potential. But in the interacting band the first transition occurs rather at 2μ as shown on the left-hand side of the figure by a blue vertical arrow which is clearly shorter in length than is the black arrow. In reality, of course, there are finite lifetime effects which broaden the initial and final states (except for the one right at the Fermi energy) and this is reflected in a rounding of the absorption edge, as do finite temperature⁴⁴ effects. In our numerical work for bare bands, we have included a small residual scattering rate on our states so that even for the red dashed curve a small rounding of the interband edge is seen in the figure. Note that this shift is also present in the previous Figs. 14 and 15.

Another feature to be noted when considering Fig. 16, is the contrast between top and bottom frame for which μ_0 goes from a value of 150 meV, which is less than $\omega_E=200$ meV, to a value of $\mu_0=400$ meV which is larger. The large value of μ_0 allows the Holstein phonon-assisted sideband to be prominently revealed. It starts at $\Omega=200$ meV in the blue curve while for the bare band it is not present. What is important to realize is that both interband and intraband processes contribute to this absorption. The intraband contribution is easily understood from conventional metal theory and arises when a photon not only induces an electronic transition, i.e., creates an excited hole-particle pair but also creates a phonon in the final state. But there is also an interband contribution to the Holstein sideband as can be seen in Fig. 17, where the total conductivity (solid black curve) is decomposed into an intraband (short-dashed blue curve) and an

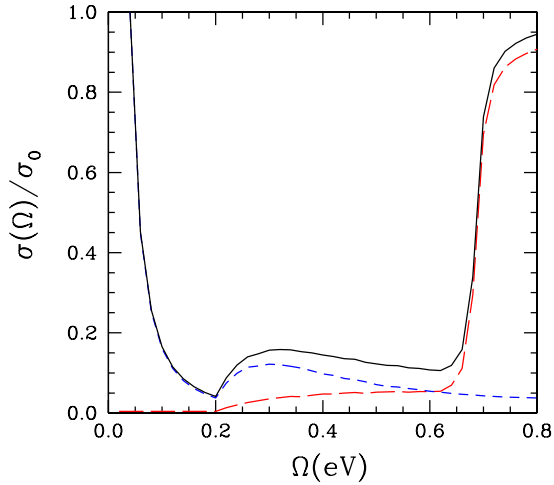


FIG. 17. (Color online) ac conductivity $\sigma(\Omega)/\sigma_0$ showing separately intraband (short-dashed blue curve) and interband (long-dashed red curve). The solid black curve is the sum of the two. The chemical potential $\mu_0=400$ meV.

interband (long-dashed red curve) contribution. To understand the behavior of the interband curve we refer to Fig. 18, where we show results for the probability of occupation of a state \mathbf{k} , $n_{\mathbf{k}}$, which can easily be calculated from the spectral density $A(\mathbf{k}, \omega)$ of Eq. (1). At finite temperature

$$n_{\mathbf{k}} = \int_{-\infty}^{\infty} f(\omega) A(\mathbf{k}, \omega) d\omega. \quad (36)$$

If, for the moment, we ignore damping effects, the electron spectral density $A(\mathbf{k}, \omega)$ becomes a delta function and the probability of occupation of a state $(\epsilon_{\mathbf{k}} - \mu_0)$ in the bare band becomes $n_{\mathbf{k}} = f[\hbar v_0(k - k_F)]$ for the $\epsilon_{\mathbf{k}} = +\hbar v_0 k$ branch and $n_{\mathbf{k}} = f[-\hbar v_0(k + k_F)]$ for the $\epsilon_{\mathbf{k}} = -\hbar v_0 k$ branch, which is just the thermal occupation function. When the EPI is included, an interesting analytical result can still be obtained if we limit ourselves to the region of small energies away from the Fermi surface. In that case, we can approximate $\text{Re } \Sigma(\omega)$ by $\text{Re } \Sigma(\omega) = -\lambda^{\text{eff}} \omega + \text{Re } \Sigma(\omega=0)$ and obtain

$$n_{\mathbf{k}} \approx \frac{1}{1 + \lambda^{\text{eff}}} f[\hbar v_0^*(k - k_F)], \quad (37)$$

where v_0^* [defined below Eq. (8)] is the renormalized effective velocity of light, k_F is the bare-band Fermi momentum and the equation is valid only for $(k - k_F)$ small. We can immediately see from Eq. (37) that the jump in occupation at the Fermi surface in the interacting system at $T=0$ has been reduced below one by the factor $1/(1 + \lambda^{\text{eff}})$. Our numerical results with and without phonons are shown in Fig. 18. The dashed blue curve is close to unity except very near the Fermi surface at $k=k_F$ in our notation. We have used a residual scattering $\eta=0.001$ meV. When phonons are included, we obtain the solid red curve which also shows a sharp drop at the Fermi surface, but the jump is now reduced below one by a factor, $1/(1 + \lambda^{\text{eff}})$, as we saw in Eq. (37). In addition, this curve has very significant tails beyond the Fermi level and at negative energies below this point, the

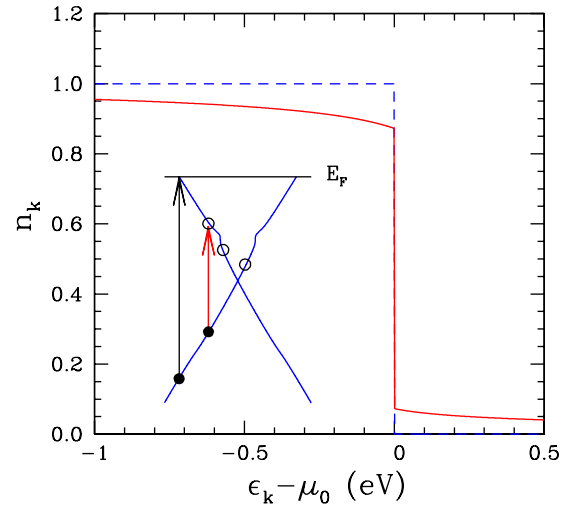


FIG. 18. (Color online) Probability of occupation of state $\epsilon_{\mathbf{k}}$ for two cases: bare band (dashed blue curve) and with electron-phonon interaction included (solid red curve). A very small residual scattering of $\eta=0.001$ eV is also present in both cases. The inset is a schematic which illustrates the renormalized energy bands filled to the Fermi level E_F with finite probability for some holes to exist below the Fermi level. Interband transitions are now possible for energies below 2μ .

probability of occupation remains reduced from the value of 1 on the scale of eV reflecting the fact that phonon renormalizations persist to high energies in graphene as we saw in Fig. 1. Thus since $n_{\mathbf{k}}$ is always less than 1, Pauli blocking is lifted on interband transitions. The initial state in the occupied lower Dirac cone of Fig. 10 remains occupied with finite probability but at the same time a final state below the Fermi level can now accommodate a photoexcited electron since this state is not occupied with probability one. This is illustrated by the inset schematic of Fig. 18, where the large black arrow represents the case where the particle is promoted to above the Fermi level, which would be a transition with minimum energy 2μ . However, the finite probability for holes to exist below the Fermi level gives rise to transitions such as shown by the short red arrow, and interband absorption can now proceed for energies which are less than 2μ . This partial lifting of Pauli blocking is responsible for the long tails extending to $\Omega=0$ seen in the lower right-hand frame of Fig. 14 which allow the interband transitions to contribute to the dc conductivity. They also allow for additional phonon-assisted interband transitions to start at $\Omega > \omega_E$ as seen in the long-dashed red curve of Fig. 17.

An interesting point to be aware of is that for large values of the chemical potential, a regime in which a Drude and its boson-assisted side bands is clearly revealed, the sidebands will not have the same relationship to the Drude as they would in a simple metal. We expect an additional contribution in this energy range from interband transitions, as shown in Fig. 17. We saw in Eq. (37) that the jump at $k=k_F$ in the occupation probability is renormalized by the EPI by a factor of $1/(1 + \lambda^{\text{eff}})$. We also saw in Fig. 18 that these renormalizations persist to high energy away from the Fermi surface and the occupation factor $n_{\mathbf{k}}$ is significantly reduced below

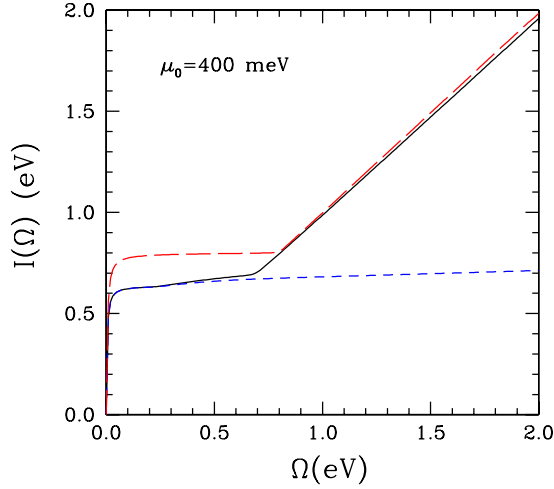


FIG. 19. (Color online) The partial optical sum $I(\Omega)$ defined in Eq. (38) vs Ω (variable upper limit on the integral). The red long-dashed curve is for the bare band case with $\eta=2.5$ meV and is for comparison. The solid black curve has phonon renormalizations. The short-dashed blue curve includes only the intraband contribution in the presence of phonon renormalizations.

one allowing for the relaxation of Pauli blocking on interband transitions. On the other hand, these renormalizations drop out of the value of the interband conductivity in Eq. (34) valid for small photon energy and Fig. 15 shows this to be true for a considerable range of energy above $\Omega=0$. This is a clear illustration that the EPI can renormalize various quantities in quite different ways.

Another interesting aspect of the redistribution of optical spectral weight that is brought about by the electron-phonon interaction is illustrated in Fig. 19 where we show the results for the partial optical sum denoted by $I(\Omega)$ and defined as

$$I(\Omega) = \int_0^{\Omega} \frac{\sigma(\Omega')}{\sigma_0} d\Omega' \quad (38)$$

with variable upper limit Ω on the integral. The red long-dashed curve is the bare-band case but with a small residual quasiparticle scattering rate $\eta=2.5$ meV included in the numerical evaluation of Eq. (21). In this case, the entire spectral weight $2\mu_0$ lost through Pauli blocking of the interband transition is found in the Drude. $I(\Omega)$ rises sharply to a height of 0.8 eV on an energy scale given by 2η , then remains constant until $\Omega=0.8$ eV $=2\mu_0$ where it starts rising again in a linear fashion. The solid black curve which includes phonons is more interesting and is to be compared with the red curve. It too rises out of zero very rapidly on the scale of η but does not go all the way up to a height of $2\mu_0$ rather it shows a saturation plateau at $2\mu_0/(1+\lambda^{\text{eff}})=2\mu$ in the region below $\omega_E=200$ meV. At ω_E , intraband and interband Holstein processes start to kick in and $I(\Omega)$ begins to rise slowly until $\Omega \sim 2\mu$ is reached where a considerable change in slope occurs because the major contribution of interband transitions starts coming in (as can be seen by comparing the blue short-dashed intraband curve with the solid black curve for the total amount). By $\omega=2\mu_0$, the black and red curves have effectively merged and the optical spec-

tral weight redistribution brought about by the EPI is in balance at this point. At larger energies $\Omega \sim 2$ eV, the solid black curve which is based on the renormalized conductivity remains below the long-dashed red curve. This is because the electron-phonon interaction has reduced the value of the universal background slightly below $\sigma_0=\pi e^2/2h$ (also seen in Fig. 16 at large Ω , where the solid blue curve is slightly below the red dashed curve).⁴⁴ This is understandable. We saw in Fig. 5 that the electron-phonon interaction has a profound effect on the band structure in the energy region around the band edge. In this region, the DOS is considerably depleted below its noninteracting value and to conserve states tails appear beyond the bare cutoff W_C . Thus in optical experiments, spectral weight is removed below the bare optical cut off which is transferred to higher energies. The slight reduction below one of the universal background is generic and we would expect it to be a feature of interactions in general.

VIII. SUMMARY AND CONCLUSIONS

It is well known^{10,11} that in wide band metals for which the band DOS is essentially constant on the scale of a few times a phonon energy, the electron-phonon interaction drops out of the renormalized DOS. Because of the Dirac nature of electron dynamics in graphene the bare-band DOS is linear in energy rather than constant and consequently an image of the phonons is retained in its dressed DOS and a first derivative of $N(\omega)$ provides an ideal baseline to study boson structures. For a bare Dirac band this derivative gives minus or plus one with the change in sign occurring at $-\mu_0$, i.e., at minus the bare chemical potential which also coincides with the Dirac point. Several modifications arise when the electron-phonon interaction is included. First, the Dirac point position is shifted and this leads to a change in the energy of the jump from minus to plus one in the first derivative. This jump remains sharp provided the chemical potential is in magnitude smaller than the phonon energy. But when the electron-phonon lifetime is finite at the Dirac point, the jump becomes smeared. In addition there are structures at $\pm\omega_E$ for an Einstein spectrum. When a distributed phonon spectrum is used, the structure in $dN(\omega)/d\omega$ reflects not only its magnitude but also its shape. With increasing doping or more precisely magnitude of chemical potential, the phonon structures are enhanced because the Fermi level falls in a region of higher density of states and consequently of larger strength of the effective electron-phonon interaction. A point of note is that at the Dirac point, the explicit logarithmic phonon structures of the finite doping case disappear, although the DOS still retains its $(1+\lambda^{\text{eff}})$ mass renormalization. Small features remain in the derivative and there is some evidence from STM (Ref. 23) for both of these effects in this limit. The method should be applicable to other scattering mechanisms such as electron-hole and plasma excitations.

Another relevant observation is that in the DOS, we find that for $\mu_0 > \omega_E$, the interactions lift the Dirac point from a value of zero in the bare case to a finite value, and that the DOS rises quadratically rather than linearly out of this point.

This is due to a finite scattering rate at the Dirac point. Recent STM experiments⁴⁵ appear to see this feature of lifting and accompanying quadratic behavior. Further investigation of this point would be warranted.

We have considered separately the effect of the EPI on the intraband and interband contributions to the optical conductivity. We find that the dc conductivity remains unrenormalized with equal contributions from both processes when the chemical potential is zero. With increasing doping through application of a gate voltage in a field-effect device or by seeding the graphene surface with potassium or other atoms, the interband contribution decreases and becomes negligible when the transport scattering rate η becomes much smaller than the chemical potential. The conditions for the observation of an universal dc limit is $\mu \ll \eta$, as well as, $T \ll \eta$. For $T > \eta$, there is a rapid increase in dc conductivity in contrast to ordinary band metals for which it is independent of temperature. For zero doping, the scale on which the universal dc value $4e^2/\pi h$ rises with increasing photon energy to its universal background value of $\pi e^2/2h$ is set by the transport scattering rate η . By contrast, but in complete parallel to what is known to apply in simple band metals, as the chemical potential is increased, a clear ac intraband Drude conductivity is revealed which is renormalized in two ways. Through analytic techniques, we show that the transport scattering rate $1/\tau$ is to be replaced by $1/[\tau(1+\lambda^{\text{eff}})]$ and the plasma frequency squared reduced to $\Omega_p^2/(1+\lambda^{\text{eff}})$. Here, λ^{eff} is the electron effective-mass renormalization at the Fermi energy which varies with doping. In addition, optical spectral weight is transferred to higher energy in the form of a Holstein phonon-assisted absorption sideband. Also, interband transitions, not part of the theory of simple metals, provide additional absorption. At small frequencies below twice the value of the chemical potential (μ) there is a small but finite nearly frequency-independent interband absorption which shows an additional Holstein side band for the case $2\mu > \omega_E$ (the phonon energy) with an additional rapid increase toward its universal background value $\sigma_0 = \pi e^2/2h$ at $\Omega \gtrsim 2\mu$. The near constant interband absorption below 2μ can be traced to a lifting of Pauli blocking brought about by the EPI. The interactions decrease the probability of occupation of a plane-wave state below the Fermi energy to a value less than one so that such states can still be used as final states for interband transitions although these are greatly reduced in optical spectral weight. In pure graphene, the increase in conductivity at $\Omega = 2\mu_0$ represents a vertical jump from 0 to σ_0 . When the EPI is included not only does the chemical-potential shift to a smaller value but the jump at 2μ is also smeared due to finite lifetime effects. While at small frequencies in the Drude region the conductivity can exceed its background value σ_0 , for energies greater than 2μ it is always slightly *smaller* than σ_0 . Consideration of the partial optical sum rule shows that missing optical spectral weight at high energy is transferred to even higher energies as compared to the bare-band case because the EPI provides states beyond the bare-band cutoff on the scale of the phonon energy. It also shows that at small energies the readjustment of optical spectral weight between bare and interacting case is in near balance at $\Omega \approx 2\mu_0$.

ACKNOWLEDGMENTS

This work has been supported by NSERC of Canada (E.J.N. and J.P.C.) and by the Canadian Institute for Advanced Research (CIFAR) (J.P.C.). S.G.S. was supported by the SCOPES Grant No. IZ73Z0_128026 of the Swiss NSF and by the Ukrainian State Foundation for Fundamental Research under Grant No. F28.2/083. He thanks V.P. Gusynin for many stimulating discussions.

APPENDIX

In this appendix, we summarize our main results and contrast them when appropriate to corresponding results in a conventional free-electron metal with constant density states on the scale of the phonon energy, in the infinite band approximation.

(1) The EPI reduces the velocity of carriers in graphene by a factor of $(1+\lambda)$ in direct analogy to the electron-mass renormalization of the quadratic dispersion curves in conventional metals.

(2) For small values of λ , the bare chemical potential μ_0 is renormalized by the same $1/(1+\lambda)$ factor. In conventional metals with particle-hole symmetry, the chemical potential remains unchanged.

(3) Also the Dirac point is shifted from $-\mu_0$ to $-\mu_0/(1+\lambda)$. In conventional metals there is no Dirac point.

(4) The shape of the electronic density of states $N(\omega)$ as a function of energy ω is altered differently by the EPI for each filling (value of chemical potential). In conventional metals, $N(\omega)$ is constant.

(5) With increased doping, the mass enhancement parameter λ can increase by more than a factor of two while in conventional metals much less change is expected for equivalent changes in free-electron density.⁵³

(6) Band edges in graphene are strongly renormalized by the EPI which provides a smearing of these edges on a scale of a few phonon energy. In conventional metals, an infinite band approximation is used.

(7) Significant phonon signatures are present in the quasiparticle density of states $N(\omega)$ versus energy even for small values of the mass-renormalization parameter λ . In conventional metals $N(\omega)$ remains constant.

(8) The first derivative of the DOS, i.e., $dN(\omega)/d\omega$, versus ω provides a picture of the underlying electron-phonon spectral density $\alpha^2F(\omega)$ and its frequency dependence. In conventional metals, this quantity is simply zero.

(9) Phonon structure appears in the ARPES renormalized dispersion curves as in ordinary metals. The shift in the chemical potential due to the EPI can however be identified. In conventional metals, there is no shift.

(10) The phonon structure in the dispersion curves increases strongly in magnitude with increasing doping while in conventional metals the corresponding changes are relatively very small.

(11) The universal dc conductivity is unrenormalized by the EPI. In conventional metals there is no universal limit but the value of the dc conductivity also remains unrenormalized.

(12) The condition for the observation of the universal limit is that the bare chemical potential be much smaller than the elastic impurity quasiparticle scattering rate η as well as $T \ll \eta$. In conventional metals, there is no universal dc limit.

(13) For $T > \eta$, there is a rapid increase in the dc value of the conductivity which originates from elastic impurity scattering. In conventional metals, the dc value limited by impurity scattering is independent of temperature.

(14) In graphene, there are both intraband and interband contributions to the ac conductivity. At the Dirac point ($\mu_0=0$ case of charge neutrality) both contributions are equal in value at $\omega=0$ but the interband transitions rapidly dominate for $\omega > \eta$ and a universal ac background appears in this frequency region. In conventional metals, there are no interband transitions in the usual infrared range of energies that are of interest. There is also no universal ac background.

(15) For larger values of chemical potential a separate Drude peak is seen in the ac conductivity followed by a region of low conductivity and then a rise toward the universal ac background value with onset at twice the value of the interacting chemical potential. In conventional metals there is only a Drude contribution.

(16) In both graphene and conventional metals, the optical spectral weight associated with the Drude piece gets renormalized downward by a factor of $(1+\lambda)$ and the effective impurity elastic-scattering rate is changed from η to $\eta/(1+\lambda)$.

(17) The interband contribution for ω and $\eta \ll \mu_0$ is constant independent of energy and unrenormalized by the EPI. In conventional metals, these transitions are not there.

(18) The electron-phonon interaction reduces slightly the universal ac background⁴⁴ below its bare value of $\sigma_0 = \pi e^2/2h$, a feature absent in conventional metals.

(19) For values of twice the chemical potential larger than the phonon energy ω_E Holstein sidebands appear beyond the Drude peak. They start at $\omega = \omega_E$ and decay for $\omega > \omega_E$ just as in ordinary metals. These sidebands, however, acquire an additional contribution from the interband transitions which are absent in a conventional metal.

(20) The partial optical sum in graphene as a function of upper cutoff Ω keeps increasing linear in Ω at high energies (but below the band edge) while in conventional metals, it would saturate at the value of the plasma frequency squared divided by 8.

*nicol@physics.uoguelph.ca

¹P. R. Wallace, Phys. Rev. **71**, 622 (1947).

²K. S. Novoselov, A. K. Geim, S. V. Morozov, D. Jiang, Y. Zhang, S. V. Dubonov, I. V. Grigorieva, and A. A. Firsov, Science **306**, 666 (2004).

³K. S. Novoselov, D. Jiang, F. Schedin, T. J. Booth, V. V. Khotkevich, S. V. Morozov, and A. K. Geim, Proc. Natl. Acad. Sci. U.S.A. **102**, 10451 (2005).

⁴K. S. Novoselov, A. K. Geim, S. V. Morozov, D. Jiang, M. I. Katsnelson, I. V. Grigorieva, S. V. Dubonov, and A. A. Firsov, Nature (London) **438**, 197 (2005).

⁵Y. Zhang, Y. W. Tan, H. L. Stormer, and P. Kim, Nature (London) **438**, 201 (2005).

⁶A. K. Geim and K. S. Novoselov, Nature Mater. **6**, 183 (2007).

⁷A. H. Castro Neto, F. Guinea, N. M. R. Peres, K. S. Novoselov, and A. K. Geim, Rev. Mod. Phys. **81**, 109 (2009).

⁸P. Carmier and D. Ullmo, Phys. Rev. B **77**, 245413 (2008).

⁹V. P. Gusynin, S. G. Sharapov, and J. P. Carbotte, Int. J. Mod. Phys. B **21**, 4611 (2007).

¹⁰G. Grimvall, *The Electron-Phonon Interaction in Metals* (North-Holland, New York, 1981).

¹¹R. E. Prange and L. P. Kadanoff, Phys. Rev. **134**, A566 (1964).

¹²B. Mitrović and J. P. Carbotte, Can. J. Phys. **61**, 758 (1983).

¹³F. Dogan and F. Marsiglio, Phys. Rev. B **68**, 165102 (2003); J. Supercond. Novel Magn. **20**, 225 (2007).

¹⁴E. Cappelluti and L. Pietronero, Phys. Rev. B **68**, 224511 (2003).

¹⁵A. Knigavko and J. P. Carbotte, Phys. Rev. B **72**, 035125 (2005).

¹⁶S. Engelsberg and J. R. Schrieffer, Phys. Rev. **131**, 993 (1963).

¹⁷T. Mori, E. J. Nicol, S. Shiiizuka, K. Kuniyasu, T. Nojima, N. Toyota, and J. P. Carbotte, Phys. Rev. B **77**, 174515 (2008).

¹⁸C. H. Park, F. Giustino, M. L. Cohen, and S. G. Louie, Phys. Rev. Lett. **99**, 086804 (2007).

¹⁹C. H. Park, F. Giustino, M. L. Cohen, and S. G. Louie, Nano Lett. **8**, 4229 (2008).

²⁰C.-H. Park, F. Giustino, C. D. Spataru, M. L. Cohen, and S. G. Louie, Phys. Rev. Lett. **102**, 076803 (2009).

²¹J. P. Carbotte, Rev. Mod. Phys. **62**, 1027 (1990).

²²E. J. Nicol and J. P. Carbotte, Phys. Rev. B **80**, 081415(R) (2009).

²³G. Li, A. Luican, and E. Y. Andrei, Phys. Rev. Lett. **102**, 176804 (2009).

²⁴M. Calandra and F. Mauri, Phys. Rev. B **76**, 205411 (2007).

²⁵A. Bostwick, T. Ohta, T. Seyller, K. Horn, and E. Rotenberg, Nat. Phys. **3**, 36 (2007).

²⁶W.-K. Tse and S. Das Sarma, Phys. Rev. Lett. **99**, 236802 (2007).

²⁷M. Polini, R. Asgari, G. Borghi, Y. Barlas, T. Pereg-Barnea, and A. H. MacDonald, Phys. Rev. B **77**, 081411(R) (2008).

²⁸J. M. Luttinger and J. C. Ward, Phys. Rev. **118**, 1417 (1960).

²⁹N. M. R. Peres, F. Guinea, and A. H. Castro Neto, Phys. Rev. B **73**, 125411 (2006).

³⁰T. Ando, X. Zheng, and H. Suzuura, J. Phys. Soc. Jpn. **71**, 1318 (2002).

³¹L. A. Falkovsky and A. H. Varlamov, Eur. Phys. J. B **56**, 281 (2007).

³²T. Stauber and N. M. R. Peres, J. Phys.: Condens. Matter **20**, 055002 (2008).

³³T. Stauber, N. M. R. Peres, and A. H. Castro Neto, Phys. Rev. B **78**, 085418 (2008); **79**, 239901(E) (2009).

³⁴N. M. R. Peres, T. Stauber, and A. H. Castro Neto, EPL **84**, 38002 (2008); **86**, 49901 (2009).

³⁵V. P. Gusynin, S. G. Sharapov, and J. P. Carbotte, Phys. Rev. Lett. **96**, 256802 (2006).

³⁶Z. Li, E. A. Henriksen, Z. Jiang, Z. Hao, M. C. Martin, P. Kim, H. L. Stormer, and D. N. Basov, Nat. Phys. **4**, 532 (2008).

- ³⁷K. F. Mak, M. Y. Sfeir, Y. Wu, C. H. Lui, J. A. Misewich, and T. F. Heinz, *Phys. Rev. Lett.* **101**, 196405 (2008).
- ³⁸F. Wang, Y. Zhang, C. Tian, C. Girit, A. Zettl, M. Crommie, and Y. R. Shen, *Science* **320**, 206 (2008).
- ³⁹T. G. Pedersen, *Phys. Rev. B* **67**, 113106 (2003).
- ⁴⁰T. Stauber, N. M. R. Peres, and A. K. Geim, *Phys. Rev. B* **78**, 085432 (2008).
- ⁴¹A. B. Kuzmenko, E. van Heumen, F. Carbone, and D. van der Marel, *Phys. Rev. Lett.* **100**, 117401 (2008).
- ⁴²R. R. Nair, P. Blake, A. N. Grigorenko, K. S. Novoselov, T. J. Booth, T. Stauber, N. M. R. Peres, and A. K. Geim, *Science* **320**, 1308 (2008).
- ⁴³M. I. Katsnelson, *EPL* **84**, 37001 (2008).
- ⁴⁴V. P. Gusynin, S. G. Sharapov, and J. P. Carbotte, *New J. Phys.* **11**, 095013 (2009).
- ⁴⁵X. Zhang, V. W. Brar, F. Wang, C. Girit, Y. Yayon, M. Panlasigui, A. Zettl, and M. F. Crommie, *Nat. Phys.* **4**, 627 (2008).
- ⁴⁶A. Knigavko, J. P. Carbotte, and F. Marsiglio, *Europhys. Lett.* **71**, 776 (2005).
- ⁴⁷M. Polini, R. Asgari, Y. Barlas, T. Pereg-Barnea, and A. H. MacDonald, *Solid State Commun.* **143**, 58 (2007).
- ⁴⁸W. L. McMillan and J. M. Rowell, *Phys. Rev. Lett.* **14**, 108 (1965).
- ⁴⁹E. Cappelluti and L. Benfatto, *Phys. Rev. B* **79**, 035419 (2009).
- ⁵⁰N. H. Shon and T. Ando, *J. Phys. Soc. Jpn.* **67**, 2421 (1998).
- ⁵¹E. V. Gorbar, V. P. Gusynin, V. A. Miransky, and I. A. Shovkovy, *Phys. Rev. B* **66**, 045108 (2002).
- ⁵²S. G. Sharapov, V. P. Gusynin, and H. Beck, *Phys. Rev. B* **67**, 144509 (2003).
- ⁵³H. K. Leung, J. P. Carbotte, D. W. Taylor, and C. R. Leavens, *Can. J. Phys.* **54**, 1585 (1976).